Developing a Generalized Model for Neutron Diffraction with Quantum Information Theory

by

Olivier Nahman-Lévesque

A thesis
presented to the University of Waterloo
in fulfilment of the
thesis requirement for the degree of
Master of Science
in
Physics (Quantum Information)

Waterloo, Ontario, Canada, 2022

Author's Declaration

This thesis consists of material all of which I authored or co-authored: see Statement of Contributions included in the thesis. This is a true copy of the thesis, including any required final revisions, as accepted by my examiners.

I understand that my thesis may be made electronically available to the public.

Statement of Contributions

Olivier Nahman-Lévesque (under the guidance of Dusan Sarenac and Dmitry Pushin) was the sole author of chapter 1, which introduces theoretical material to the thesis, chapter 3, which discusses neutron whispering gallery, as well as chapter 4, which presents possible future work. Corrections were implemented following suggestions from Dr. Alan Jamison, Dr. Dusan Sarenac and Dr. Dmitry Pushin.

This thesis contains material from two manuscripts intended for publication. Exceptions to sole authorship of material are as follows:

Research presented in Chapter 2

Sections 2.2.1-2.2.4 include materials which have been previously published in Physical Review A at the following address:

https://journals.aps.org/pra/abstract/10.1103/PhysRevA.105.022403

This research was conducted by Olivier Nahman-Lévesque in collaboration with Dr. Dmitry Pushin, Dr. Dusan Sarenac, Dr. Benjamin Heacock, Dr. Michael Huber and Dr. David Cory. The coding, figures and calculations were performed by Olivier Nahman-Lévesque. The manuscript for the publication was drafted by Olivier Nahman-Lévesque and Dr. Dusan Sarenac, with contributions from Dr. Benjamin Heacock and with all contributing authors contributing intellectual input. The appropriate statement of copyright is included for copyrighted material.

Section 2.2.5 has been submitted as a preprint which at the time of this work is awaiting publication. This research was conducted by Olivier Nahman-Lévesque in collaboration with Dr. Dmitry Pushin, Dr. Dusan Sarenac, Dr. Michael Huber and Dr. David Cory. The coding, figures and calculations were performed by Olivier Nahman-Lévesque. The manuscript for the publication was drafted by Olivier Nahman-Lévesque and Dr. Dusan Sarenac, with all contributing authors contributing intellectual input.

Abstract

Due to their high mass and neutral electric charge, neutrons are often used at low energies to probe small-scale structures or measure fundamental constants of nature. To design neutron optical elements for use in these experiments, specific crystals are used which satisfy the desired properties for the element in question such as a lens, beam splitter, or waveguide. However, the mechanics which describe the neutron-crystal interactions are governed by the equations of many-body quantum mechanics, which are often implausible to solve exactly. With some clever approximations, such as approximating the strong nuclear potential as a delta function, it is possible to describe these interactions in a way consistent with experiment to a high degree of precision. Even then, these theories are only applicable to the most basic cases, such simple geometries containing no defects. If we wish to account for diffraction effect in more complicated cases, like might be required for neutron optical devices, the systems of interest must be solved through numerical simulation.

One such a case is a situation where a neutron enters a perfect crystal close to Bragg angle. For large crystals, the theory which describes the state of the neutron as it progresses through the crystal is the theory of dynamic diffraction. While is has been verified experimentally, it fails under some circumstances such as when the crystal contains some defects or has an irregular shape. In 2016, it was observed that similar profiles to dynamical diffraction theory could be produced by looking at the intensity resulting from a one-dimensional quantum random walk. This thesis will describe how this idea can be generalized into a more complete description of the dynamical diffraction problem, which provides us with a mathematical tool to simulate the neutron state everywhere in crystals for which the standard theory is unsuitable.

In recent years, there has also been some attention given to cold neutrons diffracting in curved crystals. Rather than approaching this system as a diffraction problem, it is possible to model the crystal as a linear potential in the radial direction, which results in quantum states similar to those found in other linear potentials, such as gravity. This work will describe how these "centrifugal states" can be modeled for different experimental systems, which provides a strong theoretical baseline with which to compare experimental data.

Acknowledgements

I would like to thank my supervisor Dmitry Pushin, as well as Dusan Sarenac for their guidance with my research and for giving me the opportunity to work on these projects.

I would like to thank the members of my committee, David Cory, Kyung Soo Choi and Alan Jamison for taking the time to listen to my presentations and providing me with constructive comments.

I also received a significant amount of assistance from Dr. Benjamin Heacock, Dr. Michael G. Huber, as well as other experimental physicists at the National Institute of Standards and Technology (NIST).

Finally, I would like to thank the other students in my group, Melissa Henderson and Austin Woolverton, for their support.

Dedication

This thesis is dedicated to my parents, Silvana Nahman and Georges Lévesque, my brother, Sacha Nahman-Lévesque, as well as all of my friends.

Table of Contents

List of Figures

Chapter 1

Introduction

1.1 Background and previous work

Ever since its discovery [4], the neutron has been a staple of experimental physics, specifically as a probe the fundamental properties of quantum mechanics and materials [5, 6, 7, 8, 9, 10] as well as gravity [11] due to their neutral electric charge and small wavelength. Typical neutron experiments include small angle neutron scattering (SANS), used to study bulk magnetic properties of materials through diffraction phenomena [12, 13, 14, 15, 16, 17], triple axes spectrometry for crystal characterization [18], as well as interferometric techniques. A neutron interferometer is an apparatus in which a neutron is made to interfere with itself to quantify some property of a material, or constant of nature [19, 20, 21, 22, 23, 24, 25, 26, 27, 28, 29]. Unlike SANS techniques, interferometry conserves the phase information of the neutron, which allows for the measurement of a larger breadth of interactions. Most of these experiments make use of perfect crystals to separate the neutron current coherently into two distinct paths in physical space which are then recombined. The specific interactions between the neutron and the crystal lattice have been recently demonstrated to be of scientific interest [30, 31, 32, 33] to measure quantities such as the neutron charge radius, the neutron-electron scattering length and the structure factor of multiple materials. More recently, Mach-Zehnder type interferometers which use diffraction gratings as beam splitters have seen a rise in popularity [34, 35, 36, 37, 38] due to the lower constraints on environmental isolation. Due to this contemporary interest in neutron interferometry, there is a need for more precise neutron optical devices, which in turn would allow for more precise measurements. Efforts have been made, for example, to develop compound refractive lenses for neutrons [39, 40, 41], or other optical devices to focus a neutron

beam [42, 43, 44, 45, 46, 47, 48]. However, this endeavor poses enormous practical challenges, such as extremely precise machining and environmental isolation. Perfect crystal optical devices are showing promising results [49], however their design does not account for dynamical diffraction effects due to the computational challenge posed by DD theory for complicated geometries, or crystals containing defects and surface roughness. The goal of this work is to present a new framework through which dynamical diffraction problems can be solved computationally, which would facilitate the design of new perfect-crystal based neutron optical devices without stepping foot in a neutron reactor. We will present evidence which suggests that it is possible to create such devices with fewer limitations on crystal purity, machining, and other experimental constraints.

In 2016, it was postulated by members of our group at the University of Waterloo that quantum random walks could be used as a tool to simulate the process of diffraction [50]. The reasoning behind this observation was that since the (absorptionless) diffraction process on a microscopic level is unitary, the macroscopic process should be able to be modeled using a lattice of nodes acting upon the neutron state as a unitary matrix. Premiliminary results indicated that with the correct parameterization, the random walk process produced intensity plots similar to those observed in diffraction experiments. The contribution of this work will be to rigorously quantify the relationship between the model parameters and the experimental variables involved in a particular diffraction experiment, as well as apply the model to different geometries which are supported by experimental data.

1.2 Definitions

In quantum mechanics, the states of a quantum system can be represented as vectors in a Hilbert space H. A Hilbert space is a complete, complex inner product space with inner product

$$\langle \mathbf{v}, \mathbf{w} \rangle = z \tag{1.1}$$

where $\mathbf{v}, \mathbf{w} \in H$ and z is a complex number. The state space can be represented by a number of orthogonal basis vectors e_i which correspond to pure states, and are symbolized by the kets $|e_1\rangle, |e_2\rangle$, etc. In a two-level system (ex: the spin of spin 1/2 particle) the basis states are the up and down spin with respect to an arbitrary axis, which will be denoted z. Any pure state $|\Psi\rangle$ will be in a superposition of the basis states:

$$|\Psi\rangle = \alpha \, |\uparrow_z\rangle + \beta \, |\downarrow_z\rangle \tag{1.2}$$

where α and $\beta \in \mathbb{C}$, are defined up to a global phase factor $e^{i\theta}$ and obey the normalization condition

$$\alpha\alpha^* + \beta\beta^* = 1 \tag{1.3}$$

Every ket $|\Psi\rangle$ has an associated bra,

$$\langle\Psi| = \alpha^* \langle\uparrow_z| + \beta^* \langle\downarrow_z| \tag{1.4}$$

a linear map which maps a state $\Phi = \delta |\uparrow_z\rangle + \gamma |\downarrow_z\rangle \in H$ to the complex plane through the inner product

$$\langle\Psi|\Phi\rangle = \langle \mathbf{\Psi}, \mathbf{\Phi} \rangle \tag{1.5}$$

This inner product can be understood as taking the projection of $|\Phi\rangle$ onto $|\Psi\rangle$, and is by definition 0 when $|\Psi\rangle$ and $|\Phi\rangle$ are orthogonal and 1 when they are equal. By extension, a state $|\Psi\rangle$ can thus be represented as a column vector in $\mathbf{C}^2$, and the inner product $\langle\Psi|\Phi\rangle$ corresponds to the vector product

$$\begin{pmatrix} \alpha^* & \beta^* \end{pmatrix} \begin{pmatrix} \delta \\ \gamma \end{pmatrix} = \alpha^*\delta + \beta^*\gamma \tag{1.6}$$

Physically, this operation is closely related to the concept of a measurement. When measuring a system with respect to some basis, the quantum state collapses into one of the basis states. If a system is prepared in state $|\Phi\rangle$, then the probability p of measuring it in state $|\Psi\rangle$ is given by

$$p = |\langle\Psi|\Phi\rangle|^2 \tag{1.7}$$

where $|z|$ is the Euclidian norm of z. Therefore, the coefficients α and β in equation 1.2 can be understood as the "root" of the probability of measuring state $|\Psi\rangle$ in one of the basis states $|\uparrow_z\rangle$ or $|\downarrow_z\rangle$.

More generally, any measurable quantity is associated with a Hermitian operator (which is linear, self-adjoint and has real eigenvalues) [51]. The eigenvectors of this operator correspond to the possible states of the system after a measurement, while their respective eigenvalues correspond to the outcome of the measurement, should the system collapse in this state. The matrix representation of a given operator will depend on the chosen basis. For example, the operator associated with a spin measurement on the x axis in the previously described z basis is:

$$\hat{S}_x = \frac{\hbar}{2}\sigma_x \tag{1.8}$$

where $\hbar$ is the reduced Planck constant, and σ_x is the first Pauli matrix

$$\sigma_x = \begin{pmatrix} 0 & 1 \\ 1 & 0 \end{pmatrix} \tag{1.9}$$

This operator has two eigenvectors

$$|\uparrow_x\rangle = \frac{1}{\sqrt{2}}(|\uparrow_z\rangle + |\downarrow_z\rangle) = \frac{1}{\sqrt{2}}\begin{pmatrix}1\\1\end{pmatrix} \tag{1.10}$$

$$|\downarrow_x\rangle = \frac{1}{1\sqrt{2}}(|\uparrow_z\rangle - |\downarrow_z\rangle) = \frac{1}{\sqrt{2}}\begin{pmatrix}1\\-1\end{pmatrix} \tag{1.11}$$

with eigenvalues

$$S_{x+} = \frac{\hbar}{2} \tag{1.12}$$

$$S_{x-} = -\frac{\hbar}{2} \tag{1.13}$$

which are the two allowed values for the spin angular momentum of a spin 1/2 particle.

Finally, operators are used to represent some action which maps a state to another in the same Hilbert space. Physically, this might correspond, for example, to some rotation on a spin state inside a magnetic field. The first Pauli matrix σ_x corresponds to a state "flipping", as it interchanges the $|\uparrow_z\rangle$ and $|\downarrow_z\rangle$ states.

While the examples which have been given are limited to two dimensions, these concepts generalize to any number of dimensions. A system of two spin 1/2 particles will be described by a 4-dimensional Hilbert space, three particles: 8-dimensional, and so on. The position distribution of a single, spinless particle restricted to one dimension is represented as a vector in an infinite dimensional Hilbert space, spanned by the basis of position eigenkets $|x\rangle$:

$$|\Psi\rangle = \int \Psi(x)\,|x\rangle\,dx \tag{1.14}$$

The function $\Psi(x)$ is called the wavefunction. It related to the coefficients in 1.2 in the same way that a probability density function is related to the probability of discrete events, i.e: the probability of a particle being found between points a and b is given by

$$P_{a\leq x\leq b} = \int_a^b |\Psi(x)|^2 dx \tag{1.15}$$

it is square integrable, and normalized to 1.

1.2.1 Quantum Random Walks

Classical Random Walks

Random walks describe the path of some object through space whose movements are determined randomly in discrete time steps [52]. These are often used in classical mechanics, for example to describe the movement of a particle inside a fluid or a gas [53][54]. Generally, they are entirely described as a set of $2n$ probabilities, where n is the number of degrees of freedom of the system, with the requirement that

$$\sum_{i=1}^{2n} p_i = 1 \tag{1.16}$$

which correspond to the probability of moving in each direction at every time step.

We will concentrate on random walks in one dimension. By convention, we will imagine a particle on the number line, which can either move left or right. An "unbiased" random walk is defined such that

$$p_l = p_r = 1/2 \tag{1.17}$$

where p_l and p_r are the probabilities of moving left and right, respectively. We are interested in the probability distribution of the particle position after N steps, for arbitrary p_l and p_r. To end the walk at position n, the particle must have taken n_l steps to the left and n_r steps to the right, where $n_l + n_r = \mathrm{N}$, and $n_r - n_l = n$. n_l and n_r are therefore entirely determined by N and n like $n_r = \frac{N+n}{2}$ and $n_l = \frac{N-n}{2}$. Since the left and right steps are uncorrelated and can happen in any order, there are $\binom{N}{n_l} = \binom{N}{n_r}$ possible paths which end at position n, each happening with probability $p_l^{n_l} p_r^{n_r}$. Thus, the probability $P(n)$ of landing at position n is given by

$$P(n) = p_l^{n_l} p_r^{n_r} \binom{N}{n_l} = p_l^{n_l} p_r^{n_r} \frac{(n_r + n_l)!}{n_l! n_r!} \tag{1.18}$$

The mean position of the particle after N steps is simply the mean number of right minus left steps:

$$\langle n \rangle = N(p_r - p_l) \tag{1.19}$$

Fig. 1.1 shows two such distributions, for the unbiased case as well as for $p_l = 0.6$ and $p_r = 0.4$. The probability distribution is approximately symmetric around the mean, and moves according to $p_l - p_r$.

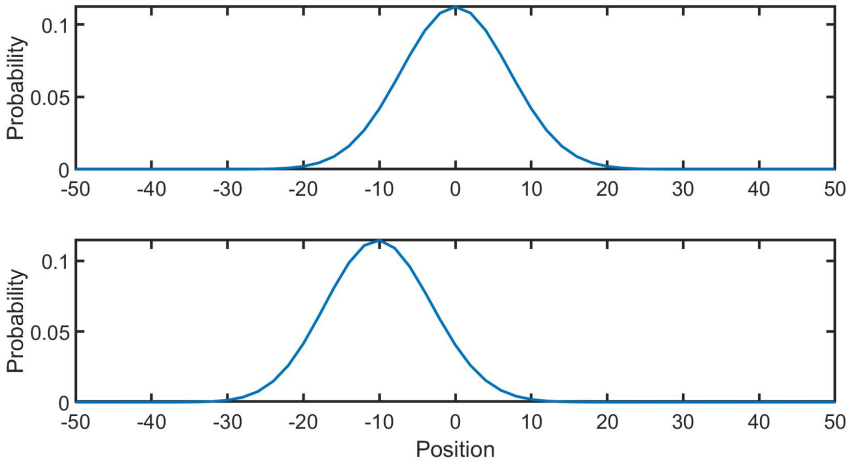

Figure 1.1: Top: the probability distribution for an unbiased classical random walk after 50 steps. The most probable outcome for the walk is 0. Bottom: the probability distribution for a classical random walk with $p_l = 0.6$ and $p_r = 0.4$. The most probable outcome is now -10, and the distribution is biased to the left.

Generalizing Into Quantum Random Walks

Quantum random walks are a generalization of this concept which make use of the properties of quantum mechanics. While a classical random walk will produce a particle at a definite position, a quantum random walk induces the particle in a superposition of position states, which once measured collapses at a definite position.

For this derivation, we follow [55]. Consider a spin $\frac{1}{2}$ particle as presented in the previous section, restricted to discrete positions in one dimension. The total state can be expressed as the tensor product of the spin 2-vector and the position state:

$$|\Psi\rangle = |s\rangle \otimes |\psi\rangle \tag{1.20}$$

where, as usual,

$$|s\rangle = \alpha \, |\uparrow_z\rangle + \beta \, |\downarrow_z\rangle \tag{1.21}$$

and the position state is given in terms of discrete allowed positions

$$|\psi\rangle = \sum_i \psi_{xi} \, |x_i\rangle \tag{1.22}$$

Eq. 1.20 can be rewritten as

$$|\Psi\rangle = \alpha\,|\uparrow_z\rangle \otimes |\psi^{\uparrow}\rangle + \beta\,|\downarrow_z\rangle \otimes |\psi^{\downarrow}\rangle \tag{1.23}$$

where $|\psi^{\uparrow}\rangle$ and $|\psi^{\downarrow}\rangle$ are the spin up and down components of the discrete position space wavefunction respectively. We now introduce a conditional shift operator

$$U = |\uparrow_z\rangle\langle\uparrow_z| \otimes \sum_i |x_{i+1}\rangle\langle x_i| + |\downarrow_z\rangle\langle\downarrow_z| \otimes \sum_i |x_{i-1}\rangle\langle x_i| \tag{1.24}$$

which shift the particle right if it has spin up

$$U\,|\uparrow_z\rangle \otimes |x_i\rangle = |\uparrow_z\rangle \otimes |x_{i+1}\rangle \tag{1.25}$$

and left if it has spin down

$$U\,|\downarrow_z\rangle \otimes |x_i\rangle = |\downarrow_z\rangle \otimes |x_{i-1}\rangle \tag{1.26}$$

If we apply the operator U to some arbitrary spin state localized at some position x_0

$$|\Psi_0\rangle = (\alpha\,|\uparrow_z\rangle + \beta\,|\downarrow_z\rangle) \otimes |x_0\rangle \tag{1.27}$$

we obtain the superposition

$$U\,|\Psi_0\rangle = \alpha\,|\uparrow_z\rangle \otimes |x_1\rangle + \beta\,|\downarrow_z\rangle \otimes |x_{-1}\rangle \tag{1.28}$$

If the state is measured in this configuration, it will collapse in either of the two available positions with the corresponding spin. If we keep applying U to the measured state and measuring between every application, the first measured state will undergo ballistic motion.

If we keep applying U over and over again, without measuring the state, the up and down spin components will keep drifting apart from each other. However, we can apply a rotation to the state between every application of U. The spin rotation operator is given by:

$$R(\theta) = \cos(\theta)\,|\uparrow_z\rangle\langle\uparrow_z| - \sin(\theta)\,|\uparrow_z\rangle\langle\downarrow_z| + \sin(\theta)\,|\downarrow_z\rangle\langle\uparrow_z| + \cos(\theta)\,|\downarrow_z\rangle\langle\downarrow_z| \tag{1.29}$$

or equivalently

$$R(\theta) = \begin{pmatrix} \cos(\theta) & -\sin(\theta) \\ \sin(\theta) & \cos(\theta) \end{pmatrix} \tag{1.30}$$

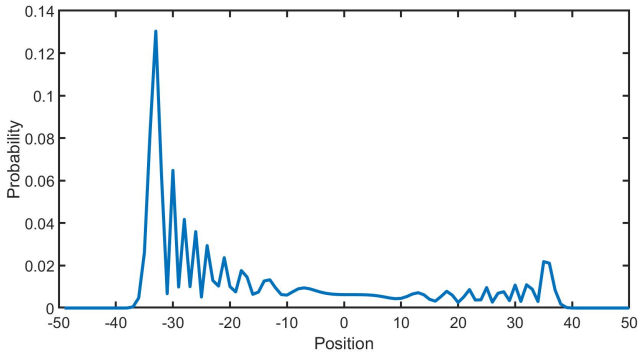

Figure 1.2: The position distribution of a spin $\frac{1}{2}$ particle initialized in the spin up state after 100 steps of an unbiased quantum random walk, using the rotation operator $R(\pi/4)$ and the shift operator U. The distribution is asymmetric due to the constructive interference on the left side.

This introduces interference between the up and down states in a strictly non-classical way, which can be observed once the state is finally measured after multiple iterations.

It is especially interesting to consider an "unbiased" operator, which gives the particle an equal chance to go left and right after a single application, since it highlights the differences between the classical and quantum behavior. In an unbiased classical walk with n steps, the position probability distribution approaches a Gaussian distribution with standard deviation $\sigma = \sqrt{N}$, as shown in Fig. 1.1. Now, one can see that substituting $\theta = \pi/4$ into Eq. 1.30 yields the unbiased rotation

$$R(\pi/4)\left|\uparrow_z\right\rangle = \begin{pmatrix} \frac{1}{\sqrt{2}} \\ \frac{1}{\sqrt{2}} \end{pmatrix} \tag{1.31}$$

Now, we start with the initial state $|\Psi_0\rangle = |\uparrow_z\rangle \otimes |x_0\rangle$ After applying the sequence of operations $UR(\pi/4)$ N times, we measure the particle's position. Before the measurement, the particle is in some superposition

$$|\Psi_f\rangle = c_{-n\uparrow}\left|\uparrow_z\right\rangle \otimes |x_{-n}\rangle + c_{-n\downarrow}\left|\downarrow_z\right\rangle \otimes |x_{-n}\rangle + c_{-n+1\uparrow}\left|\uparrow_z\right\rangle \otimes |x_{-n+1}\rangle + c_{-n+1\downarrow}\left|\downarrow_z\right\rangle \otimes |x_{-n+1}\rangle \ldots \tag{1.32}$$

Thus, the probability that it is measured at some position $|x_i\rangle$ is $|c_{i\uparrow}|^2 + |c_{i\downarrow}|^2$. Fig. 1.2 shows the position probability distribution after 100 iterations of $UR(\pi/4)$. It can easily be seen that this resembles in no fashion a Gaussian distribution, in fact it is not even symmetric. This is due to the interference between the up and down states and they

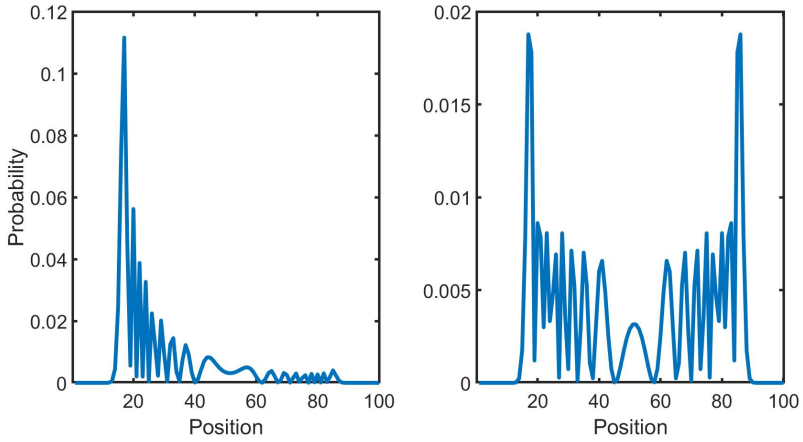

Figure 1.3: Position distribution after 100 applications of $UR(\pi/4)$ to a spin $\frac{1}{2}$ particle initialized in the spin up state, if it is first measured to be spin up (left) and spin down (right).

propagate back and forth. This is quite different from the classical expectation and is only possible because of quantum phenomena such as superposition and interference.

On a final note, if the spin is measured before the position, a different position distribution is obtained depending on the measured spin value. The two distributions are shown in Fig. 1.3.

1.3 Neutron Optics

Neutrons are a powerful tool for probing small scale structures, and have been a staple of many fundamental physics measurement over the past decades. This is due to their neutral electric charge, which allows them to interact primarily with atomic nuclei through the strong nuclear force, as well as their De Broglie wavelength:

$$\lambda_B = \frac{h}{p} \tag{1.33}$$

where h is the Planck constant and p is the relativistic momentum of a given particle. In most neutron experiments, this wavelength is usually on the order of $1 - 10$Å, which is in the same order of magnitude as many common crystal lattice constants.

The definitions in this section are derived in more detail in [56]. We start by noting that matter wave fields differ from electromagnetic wave fields in that the former are described by the Schrödinger equation

$$\left(\frac{-\hbar^2}{2m}\nabla^2 + V(\vec{r},t)\right)\Psi(\vec{r},t) = i\hbar\frac{\delta\Psi(\vec{r},t)}{\delta t} \tag{1.34}$$

as opposed to the classical wave equation

$$\nabla^2\phi(\vec{r},t) - \frac{1}{c^2}\frac{\delta^2\phi(\vec{r},t)}{\delta t^2} = 0. \tag{1.35}$$

E.M. waves always propagate at the speed of light c, whereas matter waves have a group velocity v_g, which determines the overall speed of the wave envelope, and is determined by the De Broglie relation in Eq. 1.33. However, matter waves additionally possess a phase velocity which describes the spatial rate of the change of the wave phase. Since different wavelengths travel at different velocities, a neutron which is initialized as some wavepacket

$$\psi(x,t) = \frac{1}{\sqrt{2\pi}}\int_{-\infty}^{\infty} A(k)e^{i(kx-\omega t)}dk \tag{1.36}$$

for some distribution $A(k)$ will slowly spread over space and eventually diffuse over all space.

The neutron interaction with the nucleus is effectively entirely determined by the strong nuclear force. The scale of the strong interaction is on the order of a femtometer (10^{-15}m), while the de Broglie wavelength of a typical thermal neutron is on the order of $1 - 10$ Å (10^{-10}m - 10^{-9}m). Due to this extreme difference in scale, the spatial distribution of the matter potential as seen by a neutron can be approximated as a delta function. This approximation is known as the Fermi pseudopotential, and is common practice in neutron diffraction theory. The total potential is thus a sum of Fermi pseudopotentials at each atomic site $\vec{r}_j$

$$V(\vec{r}) = \sum_j \frac{2\pi\hbar}{m} b_c \delta(\vec{r} - \vec{r}_j) \tag{1.37}$$

where the coefficient b_c is the neutron scattering length of the atom from which the scattering occurs, and δ is the Dirac delta function. Inside a magnetic material, the magnetic potential, given by

$$V_m(\vec{r}) = -\mu\vec{\sigma}\cdot\vec{B}(\vec{r}) \tag{1.38}$$

acts on the spin element of the wavefunction (spinor) through the Pauli vector

$$\vec{\sigma} = (\sigma_x, \sigma_y, \sigma_z) \tag{1.39}$$

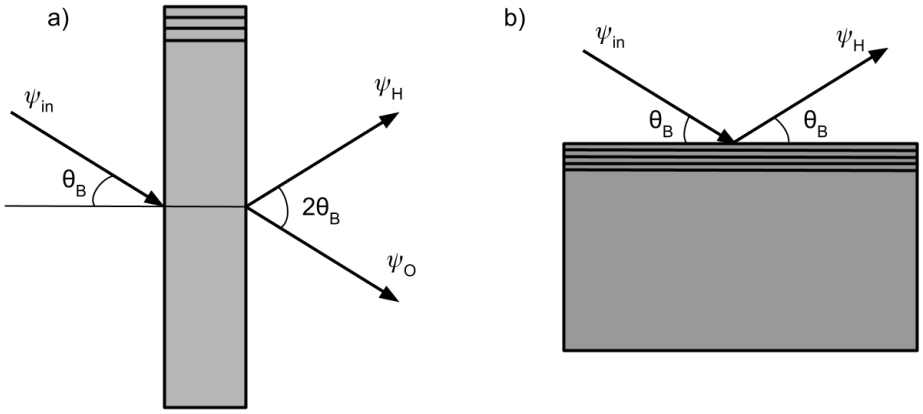

Figure 1.4: Diffraction by a crystal lattice in the Laue geometry (a) and the Bragg geometry (b).

composed of the three Pauli operators, the first of which was shown in Eq. 1.9. Finally, the neutron also feels the standard gravitational potential

$$V_g(\vec{r}) = \int m\vec{g}(\vec{r}) \cdot d\vec{r} \tag{1.40}$$

where the gravitational field $\vec{g}$ can usually be approximated as a constant, making the potential linear in position.

If the neutron state is an eigenstate of the Hamiltonian, Eq. 1.34 reduces to its time independent form:

$$\left(\frac{-\hbar^2}{2m}\nabla^2 + V(\vec{r})\right)\Psi(\vec{r}) = E\Psi(\vec{r}) \tag{1.41}$$

where E is the energy of the state. Inside a material, the spatially dependent wavevector $K(\vec{r})$ is given by

$$K^2(\vec{r}) = \frac{2m}{\hbar^2}\left(E - V(\vec{r})\right) \tag{1.42}$$

and determines the material index of refraction, defined as the ratio of the wavevector inside the material to the incident wavevector:

$$n(\vec{r}) = \frac{K(\vec{r})}{k_0} = \left(1 - \frac{V(\vec{r})}{E}\right)^{1/2} \tag{1.43}$$

which also determines the angle of propagation of a neutron beam inside the material through Snell's law

$$n = \frac{\sin(\theta_0)}{\sin(\theta_{in})} \tag{1.44}$$

where the incident beam makes an angle θ_0 with the normal to the crystal surface, which becomes θ_{in} inside the material. In general, n is complex, and its imaginary component accounts for the absorption of neutron by the material. In most cases in our interest, for non-magnetic materials, the absorption is negligible and we obtain an approximation for n by averaging over the Fermi pseudopotential in Eq. 1.37

$$n \approx 1 - \frac{\lambda^2 N b_c}{2\pi}. \tag{1.45}$$

where N is the atomic density.

An important category of neutron experimental science is experiments leveraging the concept of interferometry. Just like classical EM or mechanical waves, matter waves interfere in space depending on their frequency and phase. For a given frequency, the interaction between a neutron and its environment often induces a noticeable, deterministic phase shift. The fundamental mechanism of neutron interferometry is to separate the neutron state into multiple trajectories in physical space, induce some phase shift into a subset of these trajectories, and recombine them. The interference measured in the final state (over many neutrons) can be used to quantify these interactions with high precision.

An simple way to separate a neutron beam in two is with the use of a Laue crystal, as shown in Fig. 1.4. The action a single crystal on some neutron input state can be modeled as

$$\psi_{in} \longrightarrow t\psi_t + r\psi_r \tag{1.46}$$

where t and r are some complex transmission and reflection coefficients, with the requirement that $|t|^2 + |r|^2 = 1$, and ψ_t, ψ_r are the transmitted and reflected part of the wavefunction. Now, consider an incident neutron to a triple Laue intereferometer, initialized in state ψ_{in} as shown in Fig. 1.5. Each blade of the interferometer is a Laue crystal as described above (Bragg planes perpendicular to the incident crystal surface), and separates each part of the incoming beam in two. It can be seen that the final transmitted and reflected neutron ψ_0, ψ_H can be expressed as the sum of the paths:

$$\psi_0 = trr\psi_{trr} + rrt\psi_{rrt} \tag{1.47}$$

$$\psi_H = trt\psi_{trt} + rrr\psi_{rrr} \tag{1.48}$$

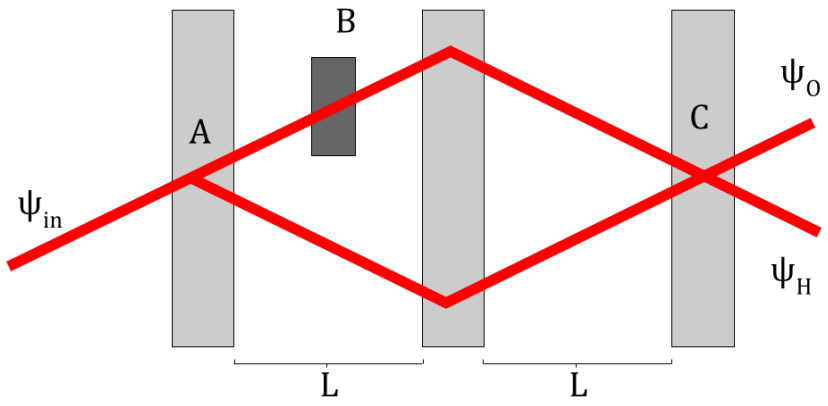

Figure 1.5: The basic geometry of a triple Laue neutron interferometer. An incoming neutron enters a crystal (A) which splits the beam into two parts. One of the paths is phase-shifted by an amount $\Delta\chi$ (B). Both parts are reflected and recombined into another beam splitter (c), resulting in a transmitted beam ψ_0 and diffracted beam ψ_H. The phase shift $\Delta\chi$ can be evaluated by looking at the relative intensities of the transmitted and reflected beam.

where, for example, ψ_{rrt} corresponds to the path undergoing a reflection on blade 1, reflection on blade 2 and transmission on blade 3. Since the beam splitter coefficients are commutative, ψ_{trr} and ψ_{rrt} are naturally in phase at the output. Since r and t are $\pi/2$ apart in phase space, ψ_{trt} and ψ_{rrr} are perfectly out of phase in an empty interferometer, and thus the H beam has intensity 0. However, it is possible to add an additional phase $\Delta\chi$ to one of the paths by adding an additional interaction (B on Fig. 1.5), which creates an asymmetry between the top and bottom paths and introduces interference in the final neutron state. With this additional phase, Eqs. 1.47 and 1.48 become:

$$\psi_0 = trr\psi_{trr}e^{\Delta\chi} + rrt\psi_{rrt} \tag{1.49}$$

$$\psi_H = trt\psi_{trt}e^{\Delta\chi} + rrr\psi_{rrr} \tag{1.50}$$

and the intensities oscillate with $\Delta\chi$ out of phase with each other

$$I_0(\Delta\chi) \propto |r|^4|t|^2\,(1+\cos(\Delta\chi)) \tag{1.51}$$

$$I_H(\Delta\chi) \propto |r|^2|t|^4 + |r|^6 - |r|^4|t|^2\cos(\Delta\chi) \tag{1.52}$$

The phase shift $\Delta\chi$ is dependent on the nature of the system interacting with the neutron at point B. For a nuclear potential such as the one in a nonmagnetic material, it is given by:

$$\Delta\chi = -Nb_c\lambda D \tag{1.53}$$

where λ is the wavelength of the neutron, D is the distance travelled though the material and N and b_c are the same as in Eq. 1.45. In a magnetic field

$$\Delta\chi = \pm\frac{\mu B m\lambda D}{2\pi\hbar^2} \tag{1.54}$$

where B is the magnetic field strength, μ is the magnetic moment of the neutron, m is neutron mass, and D is the distance travelled inside the magnetic field. The sign of the phase shift depends on the spin of the incident neutron. In a gravitational potential, things are slightly trickier as the whole interferometer setup will most likely be basking in the same potential (or at least can be approximated as such). Thus, the phase shift has a dependence of the total area between the beams A, and is given as:

$$\Delta\chi = \frac{m^2 g\lambda A\sin\alpha}{2\pi h^2} \tag{1.55}$$

where g is the gravitational acceleration, α is the angle between the area of interaction and the horizontal plane, and h is the Planck constant. Due to our ability to measure this phase

shift, neutron interferometers are an extremely powerful tool to probe to systems which are otherwise difficult to measure. They could in theory be used to measure with high precision the gravitational constant of the Earth, the neutron magnetic moment and many other quantities of interest, although there are experimental challenges yet to be resolved. Due to the weak nature of the gravitational and magnetic interaction for neutrons, any such measurement would require precision levels above anything previously achieved previously.

Chapter 2

Dynamical Diffraction and the Quantum Information Model

Neutron diffraction through perfect crystals is a complicated problem. To solve this problem exactly, one has to consider the interaction of the incident neutron with every single particle across its trajectory as its wavefunction expands through space. This is unfeasible computationally, and thus the problem must be simplified. Instead of considering the scattering from the individual atoms, the crystal can be described as an array of planes, called Bragg planes from which the neutron reflects, with reflectivity determined by its incident angle. The angle which yields the highest reflectivity is called the Bragg angle, and is given by:

$$\theta_B = \sin^{-1}\left(\frac{n\lambda}{2d}\right) \tag{2.1}$$

where n is the diffraction order, λ is the wavelength of the incident wave, and d is the lattice spacing of the crystal.

Historically, this problem has been tackled by tactically neglecting multiple scattering inside the crystal (first Born approximation). This is described by the kinematic theory of diffraction, which predicts that the intensity of the diffracted wave is proportional to the volume of the crystal. This is a good approximation for thin crystals, but gets increasingly worse as the crystal thickness is made bigger, as the intensity is uncapped and is predicted to grow infinitely as the volume goes up. A more complete, but many times more complex

theory which accounts for multiple scattering was developed over the course of the 20$^{\text{th}}$ century, including work from Cowley and Moodie [57], Zachariasen [58], Kato [59] and more. This theory, dubbed the dynamical theory of diffraction (DD) is quite extensive and will not be presented fully in this thesis, however some important points will be noted. In an experimental setting, a neutron beam is usually directed at the crystal at some angle θ_0 with respect to the crystal face. Some fraction of the neutrons will propagate straight through, and the rest will be diffracted at some angle, which depends on the Bragg condition. The two outgoing beams are called the transmitted and diffracted beam, respectively. The neutron inside the crystal is described as four mutually interfering wavefronts, two propagating in each of the beam directions. The neutron intensity propagates back and forth between the transmitted and diffracted beam with period Δ_H, called the Pendellösung period, given by

$$\Delta_H = \frac{\pi V_{cell} \cos\theta_B}{\lambda |F_H|} \tag{2.2}$$

where V_{cell} is the volume of a crystal unit cell, θ_B is the Bragg angle, λ is the neutron wavelength and F_H is the crystal structure factor.

2.1 The Takagi-Taupin equations

In the standard theory of dynamical diffraction, the incident neutron wavefunction is usually described as a plane wave

$$\Psi(\mathbf{r}) = A_0 e^{i\mathbf{k_0}\cdot\mathbf{r}} \tag{2.3}$$

where A_0 is the incident amplitude, k_0 is the incident wavevector and r is the spherical position coordinate. However, this is an inadequate description for most experiments, since a neutron beam will most likely be collimated through a slit. The Takagi-Taupin (T-T) equations are an alternate approach to dynamical diffraction problems in which we are free to specify the state of the incident neutron as the initial condition to a differential equation. The expressions derived by the T-T equations are central to the work presented in this thesis, so they will be descried in further detail. The following derivation follows [56].

The incident beam is determined by a central wavevector $\mathbf{K_0}$, which satisfies the Bragg condition with respect to a reciprocal lattice vector $\mathbf{H}$. $\mathbf{H}$ is normal to the lattice planes, which are separated by a constant distance $d = 2\pi/H$. From the Bragg condition, the reflected wave will have wavevector $\mathbf{K_0} + \mathbf{H}$. Inside the crystal, the neutron wavefunction must be a solution to the time-dependent Schrödinger equation

$$(\nabla^2 + k_0^2)\psi(\mathbf{r}) = \nu(\mathbf{r})\psi(\mathbf{r}) \tag{2.4}$$

where

$$\nu(\mathbf{r}) = \frac{2m}{\hbar^2} V(\mathbf{r}) \tag{2.5}$$

is the scaled periodic potential. It can be expressed in terms of its Fourier components

$$\nu(\mathbf{r}) = \sum_{H'} \nu_{H'} e^{i\mathbf{H'}\cdot\mathbf{r}} \tag{2.6}$$

where the component $\nu_{\mathbf{H'}}$ corresponds to the reciprocal lattice vector $\mathbf{H'}$. However, the reflected wave is almost entirely determined by the components corresponding to the reciprocal lattice vector $\pm\mathbf{H}$, and thus the potential can be approximated

$$\nu(\mathbf{r}) = \nu_0 + \nu'_{\mathbf{H}} e^{i\mathbf{H}\cdot\mathbf{r}} + \nu'_{-\mathbf{H}} e^{-i\mathbf{H}\cdot\mathbf{r}} \tag{2.7}$$

The potential can also be expressed in terms of the Fermi pseudo-potentials of the atoms in the crystal

$$\nu(\mathbf{r}) = 4\pi \sum_j b_j \delta(\mathbf{r} - \mathbf{r_j}) \tag{2.8}$$

Where b_j is the scattering length of atom j and δ is the Dirac delta function. Equating the two expressions for $\nu(\mathbf{r})$:

$$\begin{aligned} \nu_0 + \nu'_{\mathbf{H}} e^{i\mathbf{H}\cdot\mathbf{r}} + \nu'_{-\mathbf{H}} e^{-i\mathbf{H}\cdot\mathbf{r}} &= 4\pi \sum_j b_j \delta(\mathbf{r} - \mathbf{r_j}) \\ \nu_0 e^{-i\mathbf{H}\cdot\mathbf{r}} + \nu'_{\mathbf{H}} + \nu'_{-\mathbf{H}} e^{-2i\mathbf{H}\cdot\mathbf{r}} &= 4\pi \sum_j b_j e^{-i\mathbf{H}\cdot\mathbf{r}} \delta(\mathbf{r} - \mathbf{r_j}) \end{aligned} \tag{2.9}$$

We now integrate over the volume of one crystal unit cell

$$\frac{1}{4\pi} \int_{V_{cell}} \nu_0 e^{-i\mathbf{H}\cdot\mathbf{r}} + \nu'_{\mathbf{H}} + \nu'_{-\mathbf{H}} e^{-2i\mathbf{H}\cdot\mathbf{r}} dV = \sum_{j=1}^{N} b_j e^{-i\mathbf{H}\cdot\mathbf{r_j}} \tag{2.10}$$

where the sum now runs over the atoms in one unit cell. The right hand side is known as the structure factor F_H of the crystal, by definition. For the left hand side, it can be understood heuristically that the ν_0 and $\nu_{-\mathbf{H}}$ terms integrate to 0. This is due to the nature of $\mathbf{H}$ being a reciprocal lattice vector, at the edge of the unit cell $\mathbf{H}\cdot\mathbf{r} = 2\pi$, and the integral goes to 0. Thus, we are left with

$$\nu'_{\mathbf{H}} = \frac{4\pi F_H}{V_{cell}} \tag{2.11}$$

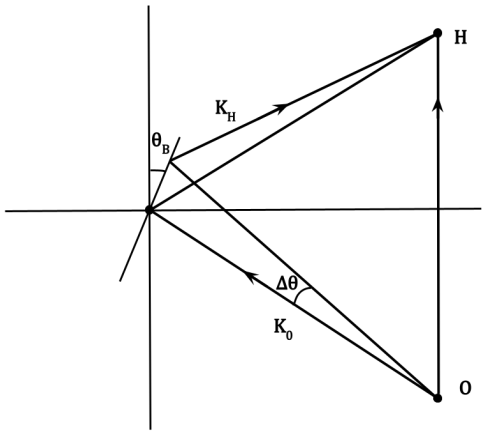

Figure 2.1: The vectors in reciprocal lattice space used in the Takagi-Taupin equations. When the incoming wave is perfectly on Bragg, the incoming wavevector $\mathbf{K_0}$ and the diffracted wavevector $\mathbf{K_H}$ fulfill the Bragg condition, $\mathbf{K_0} + \mathbf{K_H} = \mathbf{H}$. In practice, the incoming wave has a small misset angle $\Delta\theta$, and the effective $\mathbf{K_H}$ is slightly offset.

where V_{cell} is the volume of one crystal unit cell. For convenience, we define the reduced potential component

$$\nu_{\mathbf{H}} = \frac{\nu'_{\mathbf{H}}}{2k_0} \tag{2.12}$$

Inside the crystal, the neutron wavefield can be presented in the form of a sum of plane waves (wavepacket)

$$\psi(\mathbf{r}) = \sum_h \psi_h e^{i\mathbf{K}_h \cdot \mathbf{r}} \tag{2.13}$$

where the sum runs over all the reciprocal lattice vectors h, K_h are the wave vectors $K_h = K_0 + h$ and K_0 is the central wave vector of the incident beam. In the principal case of interest where the wavefield is composed of two strong waves in the incident and diffracted direction, equation 2.13 becomes

$$\psi(\mathbf{r}) = \psi_0 e^{i\mathbf{K}_0 \cdot \mathbf{r}} + \psi_H e^{i\mathbf{K}_H \cdot \mathbf{r}} \tag{2.14}$$

We now assume that the coefficients ψ_0, ψ_H are slowly varying functions of position. As shown in Fig. 2.1, the magnitude of $\mathbf{K_H}$ differs slightly from that of $\mathbf{K_0}$, and is approximately given by:

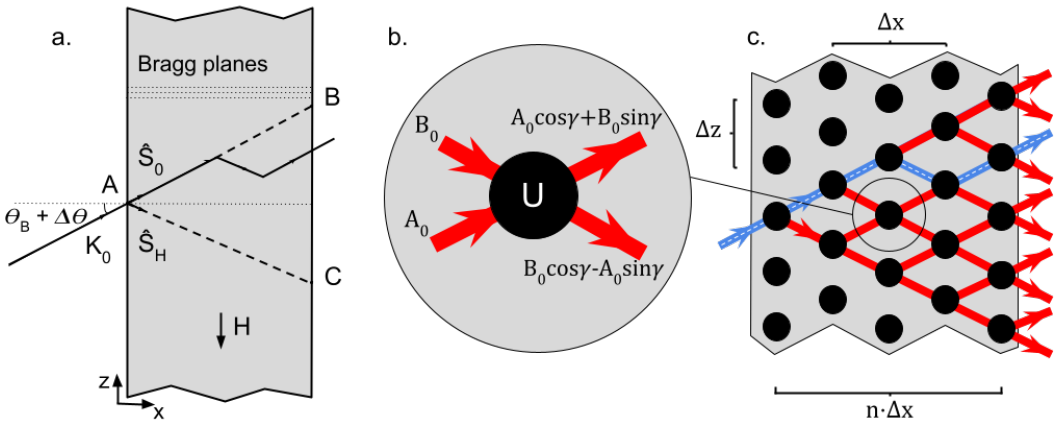

Figure 2.2: A side to side comparison of the Laue diffraction geometry in crystals with the mechanism behind the QI model for DD, in the Laue case. a. The real-space coordinates used in the Takagi-Taupin equations. An incident neutron with wavevector K_0 hits the crystal at a slight deviation from Bragg angle $\theta_B + \Delta\theta$. The coordinates $\hat{S}_0$, $\hat{S}_H$ are unit vectors in the incident and diffracted directions, respectively. b. The individual nodes act as a quantum unitary gate which splits the incident beam according to the model parameter γ. c. The diffracted amplitude at a given node is composed of the summed amplitudes of all the paths which end in the diffracted direction at that node. The widths Δx, Δz correspond to the size of the lattice spacing in simulations. Illustrated in blue (dashed) is a sample path through the lattice, which undergoes two reflections. Previously published in [1]. © 2022 American Physical Society

$$K_H^2 \approx K_0^2[1 - 2\Delta\theta \sin(2\theta_B)] \tag{2.15}$$

where $\Delta\theta$ is the deviation of the incident beam angle from the Bragg angle.

We can now define the coordinate vectors S_0, S_H as shown in Fig.2.2

$$S_0 = \frac{1}{2}\left(\frac{x}{\cos\theta_B} + \frac{z}{\sin\theta_B}\right) \tag{2.16}$$

$$S_H = \frac{1}{2}\left(\frac{x}{\cos\theta_B} - \frac{z}{\sin\theta_B}\right) \tag{2.17}$$

as the spatial coordinates parallel to the direction of K_0, K_H. Plugging the wavefunction 2.14 into the Schrödinger equation 2.4 and solving for the coefficient to the exponentials,

we obtain the pair of differential equations

$$-\nu_0\psi_0 + i\frac{\delta\psi_0}{\delta S_0} - \nu_{-H}\psi_H = 0 \tag{2.18}$$

$$-\nu_H\psi_0 + i\frac{\delta\psi_H}{\delta S_H} - (\beta - \nu_0)\psi_H = 0 \tag{2.19}$$

where $\beta = K_0\Delta\theta\sin(2\theta_B)$. The ∇^2 order terms have been neglected, and $\mathbf{K_0}$ and $\mathbf{K_H}$ are assumed to be practically parallel to the $\hat{S_0}$ and $\hat{S_H}$ directions ($\Delta\theta$ is small). We now make an ansatz on the amplitudes $\psi_{0,H}$

$$\psi_0(S_0, S_H) = e^{-i\nu_0(S_0+S_H)+i\beta S_H}U_0(S_0, S_H) \tag{2.20}$$

$$\psi_H(S_0, S_H) = e^{-i\nu_0(S_0+S_H)+i\beta S_H}U_H(S_0, S_H) \tag{2.21}$$

where the functions $U_{0,H}$ are simply the transmitted and diffracted amplitudes, up to a position-dependant phase. Substituting equations 2.20 and 2.21 into 2.19 yields the Takagi-Taupin equations:

$$\frac{\partial U_0}{\partial S_0} = -i\nu_{-H}U_H \tag{2.22}$$

$$\frac{\partial U_H}{\partial S_H} = -i\nu_H U_0 \tag{2.23}$$

This pair of differential equations describes the amplitude current between the two principal waves inside the crystal as they are continuously scattered back into each other. One could imagine that to solve these equations numerically, we would determine some initial conditions on $U_{0,H}$ and keep track of their value while proceeding in small increments of position. This is the general idea behind the quantum information model which will be presented in this thesis. These equations were solved by Werner *et al.* in 1986 [60]. The general solution for U_H is

$$U_H(S_0, S_H) = \sum_{n=-\infty}^{\infty} a_n \left(\frac{S_0}{S_H}\right)^{n/2} \mathrm{J}_n\left(2\nu\sqrt{S_0 S_H}\right) \tag{2.24}$$

where J_n is the n^{th} Bessel function of the first kind, $\nu^2 = \nu_H\nu_{-H}$, and the coefficients a_n are determined by the initial conditions. In the case where the incident beam is confined to a very narrow slit close to the entrance edge of the crystal, the incident beam can be described by the wavefunction

$$\psi_i(r) = A_0\delta(S_H)e^{iK_0\cdot r} \tag{2.25}$$

where δ is the Dirac delta function. Using this function as an initial condition, the solution to equations 2.22 and 2.23 becomes

$$U_H(S_0, S_H) = -i\nu_H \mathrm{J}_0\left(2\nu\sqrt{S_0 S_H}\right) \tag{2.26}$$

$$U_0(S_0, S_H) = \nu\sqrt{\frac{S_0}{S_H}}\mathrm{J}_1\left(2\nu\sqrt{S_0 S_H}\right) \tag{2.27}$$

The intensity profile of the neutron after being diffracted through a crystal was measured by Shull [61] by scanning the edge with a narrow slit and counting them as a function of position. To determine what one could measure with such a setup in the case of our incident beam, we must determine the intensity at $x = D$, the crystal thickness. Rather than express the intensity as a function of z, it is more convenient to define the parameter

$$\Gamma = \frac{z}{D\tan\theta_B} \tag{2.28}$$

and the intensities at $x = D$ are found to be

$$I_H(\Gamma) = \nu^2|A_0|^2\mathrm{J}_0\left(\pi\frac{D}{\Delta_H}\sqrt{1-\Gamma^2}\right)^2 \tag{2.29}$$

$$I_0(\Gamma) = \nu^2|A_0|^2\frac{1-\Gamma}{1+\Gamma}\mathrm{J}_1\left(\pi\frac{D}{\Delta_H}\sqrt{1-\Gamma^2}\right)^2 \tag{2.30}$$

where the constant Δ_H is the period of the Pendellösung interference effects inside the crystal, and can be expressed in terms of experimental variables as follows

$$\Delta_H = \frac{\pi V_{cell}\cos\theta_B}{\lambda|F_H|} \tag{2.31}$$

In typical intereferometry experiments which use perfect crystals as beam splitters, dynamical diffraction effects are not taken into consideration, due to their negligible contribution. However, it is possible that these effects become important in high precision measurements; the properties of DD could potentially be leveraged to develop new neutron optical instruments. However, the theory presented in this section lends itself poorly to more complicated systems, since the T-T equations cannot be solved if the crystal is locally imperfect, or if it is cut in a more complicated geometry. One of our objectives is to develop a numerical model for DD which could help with the design of such interferometry experiments, by precisely quantifying DD effects in complex geometries.

2.2 The Quantum Information Model for Dynamical Diffraction

2.2.1 Model description

Quantum random walk (QRW) theory is well established, and has been summarily presented in the introduction to this work. The original proposition of using these QRW to model particle diffraction was presented by Nsofini *et al.* [50]. In this section, we will describe the underlying mechanisms of the model, as well as the specific implementation which we have used in the simulations that follow.

In the model, a perfect crystal is represented as a two-dimensional lattice of nodes, through which the incident neutron travels column by column. As shown in Fig. 2.2b and 2.2c, each node acts as a unitary operator on one part of the neutron's state, which is composed of a superposition of upwards and downwards paths at every position in the lattice. Each node corresponds to the action of one or many lattice planes upon an incident neutron, with the physical size of the node being determined by the choice of parameters. The input state to a node at position i is represented by

$$\alpha_i \left|a_i\right\rangle + \beta_i \left|b_i\right\rangle \quad \text{or} \quad \begin{pmatrix} \alpha_i \\ \beta_i \end{pmatrix} \tag{2.32}$$

where $|a_i\rangle$ and $|b_i\rangle$ are the states of the neutron going upwards (transmitted) and downwards (reflected), respectively. Evolution of the initial state is performed via the unitary time evolution operator in the interaction picture $U = e^{-i\int V(r)dt/\hbar}$, where $V(r)$ is the interaction potential representing the lattice, which appears on the right hand side of Eq. 2.5. The potential integrated over the time it takes a neutron to pass through a single node is

$$\langle a|V(r)|b\rangle \frac{\Delta t}{\hbar} = \pi/2 \frac{\Delta x}{\Delta_H} e^{i\boldsymbol{H}\cdot\boldsymbol{r}} = \gamma\, i e^{i\zeta} \tag{2.33}$$

where $\Delta x = 2m\,\Delta t/(\hbar K_x)$ is twice the distance between nodes along the Bragg planes (Figs. 2.2c and 2.3) with $K_x = (2\pi/\lambda)\cos\theta_B$ the component of internal neutron wavevector also along the Bragg planes; and the phase factor encodes the global translation of the lattice. The extra factor of i is inserted for convenience and corresponds to translating the lattice by one fourth of the Bragg plane spacing. Noting that $\langle a|V(r)|b\rangle = \langle b|V(r)|a\rangle^*$, the full time-evolution operator over one node $U_i = e^{-i\int \mathcal{H}dt/\hbar}$ is

$$U_i = \sum_{n=0}^{\infty} \frac{1}{n!} \begin{pmatrix} 0 & \gamma\, e^{i\zeta} \\ -\gamma\, e^{-i\zeta} & 0 \end{pmatrix}^n$$
$$U_i = \begin{pmatrix} \cos\gamma & e^{i\zeta}\sin\gamma \\ -e^{-i\zeta}\sin\gamma & \cos\gamma \end{pmatrix} \tag{2.34}$$

The unitary describing neutron propagation to the next layer of nodes

$$U_i = |a_{i+1}\rangle \left(t_a \langle a_i| + r_b \langle b_i|\right) + |b_{i-1}\rangle \left(r_a \langle a_i| + t_b \langle b_i|\right) \tag{2.35}$$

is a slight generalization of the operator $UR(\theta)$ presented in section 1.2.1. It follows from Eq. 2.34 that it has coefficients

$$\begin{aligned} t_a = e^{i\xi}\cos\gamma, \quad r_b = e^{i\zeta}\sin\gamma \\ r_a = -e^{-i\zeta}\sin\gamma, \quad t_b = e^{-i\xi}\cos\gamma \end{aligned} \tag{2.36}$$

which necessarily adhere to the required normalization conditions of a unitary matrix

$$|t_a|^2 + |r_a|^2 = 1, \ |t_b|^2 + |r_b|^2 = 1, \ t_a\overline{r_b} + r_a\overline{t_b} = 0. \tag{2.37}$$

The phase ξ on the diagonals is not physical and thus set to zero. The off-diagonal phase ζ associated with a global lattice translation is important to interferometer simulations [62, 63], where a relative translation of one of the diffracting optics shifts the phase of the measured interference pattern, but it is of no consequence to the simulations presented here and also set to zero.

The input to one column containing h nodes is

$$\psi_{in} = \begin{pmatrix} \alpha_i \\ \beta_i \end{pmatrix}^{\otimes h} \tag{2.38}$$

where α_i, β_i are the inputs in the transmitted and reflected direction to the i^{th} node. For

calculation purposes, this is written as

$$\psi_{in} = \begin{pmatrix} \vdots \\ \alpha_i \\ \beta_i \\ \alpha_{i+1} \\ \beta_{i+1} \\ \vdots \end{pmatrix} \tag{2.39}$$

The column operator $U_i^{\otimes h}$ is represented as a matrix, where every node has matrix representation

$$M_i = \begin{pmatrix} t_a & r_b \\ 0 & 0 \\ 0 & 0 \\ r_a & t_b \end{pmatrix} \tag{2.40}$$

and the full column operator is written as:

$$C = \begin{pmatrix} \boxed{\begin{matrix} t_a & r_b \\ 0 & 0 \\ 0 & 0 \\ r_a & t_b \end{matrix}} & \boxed{\begin{matrix} 0 & 0 \\ 0 & 0 \\ t_a & r_b \\ 0 & 0 \end{matrix}} & \cdots \\ \begin{matrix} 0 & 0 \\ 0 & 0 \end{matrix} & \boxed{\begin{matrix} 0 & 0 \\ 0 & 0 \\ r_a & t_b \end{matrix}} & \\ \vdots & & \ddots \end{pmatrix} \tag{2.41}$$

For a crystal with a thickness of N nodes, the output ψ_{out} is equal to $C^N\psi_{in}$, where the odd entries of ψ_{out} correspond to the transmitted beam at each node and the even entries to the reflected beam. The beam profiles are given by discrete functions of the node height j:

$$I_H(j) = |\psi_{\text{out}}(2j)|^2 \tag{2.42}$$

$$I_0(j) = |\psi_{\text{out}}(2j-1)|^2 \tag{2.43}$$

2.2.2 Generalization of QI model to arbitrary parameters

It has been shown previously in [50] that propagating a neutron inside a lattice by exciting a single node at the entrance yielded intensity profiles consistent with dynamic diffraction

theory, with accuracy for a specific choice of γ depending on the number of layers used in the simulation. Here, we generalize this theory to any value of γ, and show that one has a degree of freedom when choosing a combination of γ and the number of iterations in the simulation (n). Furthermore, we show that the intensity profiles generated by the model exactly reduce to the spherical wave solutions of the T-T equations, equations 2.29 and 2.30, in the appropriate limit.

To demonstrate this, we determine analytically the intensity profiles predicted by the model at the exit face of the crystal. In [52], Chandrasekhar discusses the reduction of random walks with large number of steps into differential equations. In this section, we will go in the opposite direction, and show that the Takagi-Taupin equations can be reduced to a simple set of rules for a quantum random walk, with large enough number of steps.

In Fig. 2.2c, in blue, a path is shown through a lattice of width $n = 2$, starting at $p = 0$ (by definition) and ending on node $p = 1$. The total neutron amplitude at $p = 1$ will be a sum of the contributions from all the paths ending on that node, and thus the problem of calculating intensity profiles can be reduced to counting lattice paths. We will start by noting that counting the number of paths of half-length n ending at node p is equivalent to counting the number of binary words of length $2n$ with exactly $n + p$ zeros and $n - p$ ones, where these numbers represent an up or down movement, respectively (for example, the aforementioned path corresponds to the string 0010). Since there are $n + p$ choices for the positions of the zeros, there are $2n$ choose $n + p$

$$N(p) = \binom{2n}{n+p} \tag{2.44}$$

such paths.

However, not all paths contribute equally to the final amplitude, and a given path's weight will depend on the number of reflections which it undergoes. Instead of simply counting the paths which end on a specific node, we must additionally keep track of their number of reflections.

We can uniquely represent a path P as a list $\vec{v}$ where each element corresponds to the number of half-steps before a reflection occurs. A reflection on the first node is shown as a 0 in the first entry of $\vec{v}$, and the final node does not contribute to the list. As an example, the path shown in blue in figure 2.2 corresponds to the list $[2, 1, 1]$. Since the path has been pre-determined to start in the upwards direction, by definition of a reflection the odd elements of $\vec{v}$ correspond to motion upwards, and the even elements to motion in the downwards direction. By inspection, we observe that a list $\vec{v_P}$ corresponding to a path P of length $2n$ with k reflections will have $k + 1$ elements. The requirement that the path

must start on the central nodes and end on node p corresponds to the following constraint: the odd entries of $\vec{v}$ must add to $n+p$. The even entries must add to $n-p$.

For even k, there are $k/2+1$ odd entries and $k/2$ even entries. Let us note quickly that an integer N can be partitioned into exactly K nonzero integers in $\binom{N-1}{K-1}$ different ways. Now, the odd elements of $\vec{v}$ must add to $n+p$, however the first element can either be a zero or not. If it is, then $n+p$ must be partitioned into $k/2$ parts. If not, then it must be partitioned into $k/2-1$ parts instead. In total, there are

$$\binom{n+p-1}{k/2} + \binom{n+p-1}{k/2-1} = \binom{n+p}{k/2} \tag{2.45}$$

possible arrangements. The even elements of $\vec{v}$ are all strictly larger than 0, and so there are $\binom{n-p-1}{k/2-1}$ possible arrangements for them. Since the even and odd elements are independent, in total there are $\binom{n+p}{k/2}\binom{n-p-1}{k/2-1}$ possibilities for $\vec{v}$.

For odd k, there are instead $(k+1)/2$ odd entries and $(k+1)/2$ even entries. Applying a similar logic, we find that the total number of possibilities for $\vec{v}$ is $\binom{n-p-1}{(k-1)/2}\binom{n+p}{(k-1)/2}$. In summary, the number of paths ending on node p of length $2n$ with k reflections $N(n,k,p)$ is:

$$N(n,k,p) = \begin{cases} \binom{n-p-1}{k/2-1}\binom{n+p}{k/2} & k \text{ even} \\ \binom{n-p-1}{(k-1)/2}\binom{n+p}{(k-1)/2} & k \text{ odd} \end{cases} \tag{2.46}$$

or, alternatively, for arbitrary k

$$N(n,2k,p) = \binom{n-p-1}{k-1}\binom{n+p}{k} \tag{2.47}$$

$$N(n,2k+1,p) = \binom{n-p-1}{k}\binom{n+p}{k} \tag{2.48}$$

Summing over all the paths ending at node p and giving every path the appropriate amplitudes from equation 2.36 gives us the expression for the neutron amplitude profile at the exit face of the crystal. The same paths contribute to the diffracted and transmitted intensities, up to one final reflection on the last layer. The diffracted and transmitted

amplitude profile are found to be

$$\psi_H(p,n) = \sum_{k=0}^{n-|p|} (-1)^{k+1} \sin^{2k+1}\gamma \cos^{2(n-k)}\gamma \times \binom{n+p}{k}\binom{n-p}{k} \tag{2.49}$$

$$\psi_0(p,n) = \sum_{k=0}^{n-|p|} (-1)^{k} \sin^{2k}\gamma \cos^{2(n-k)+1}\gamma \times \binom{n-p-1}{k-1}\binom{n+p+1}{k} \tag{2.50}$$

$\psi(p)$ ranges from $p = -n$ to $p = n$. For small n, $\psi(p)$ has a low resolution and is a poor match to the theoretical predictions. To increase the resolution of ψ while keeping the crystal thickness finite, it is necessary to ensure that the scale of the interactions decreases proportionally, so that the effective thickness of the crystal remains constant. This can be achieved by considering the limit where $\gamma \to 0$ and $n \cdot \gamma$ is kept constant.

To show this, we expand the binomial coefficients, and rearrange some terms. Starting with the reflected beam:

$$I_H(p) = \left[(-1)\sin\gamma\cos^{2n}\gamma \sum_{k=0}^{n-|p|} \left((-1)^k \tan^{2k}\gamma\right) \left(\frac{(n+p)!(n-p)!}{k!^2(n+p-k)!(n-p-k)!} \right) \right]^2 \tag{2.51}$$

The expression $\frac{(n+p)!(n-p)!}{(n+p-k)!(n-p-k)!}$ can be expanded using Stirling's approximation, $n! = \sqrt{2\pi n}(n/e)^n$ to obtain

$$\sqrt{\frac{(n-p)(n+p)}{(n-p-k)(n+p-k)}} \left(\frac{n-p}{e}\right)^{n-p} \left(\frac{n+p}{e}\right)^{n+p} \times \left(\frac{n-p-k}{e}\right)^{-(n-p-k)} \left(\frac{n+p-k}{e}\right)^{-(n+p-k)}$$

which simplifies to

$$\sqrt{\frac{n^2-p^2}{n^2-2nk+k^2-p^2}} \left(\frac{n-p}{n-p-k}\right)^{n-p} \left(\frac{n+p}{n+p-k}\right)^{n+p} \left(\frac{n^2-2nk+k^2-p^2}{e^2}\right)^{k} \tag{2.52}$$

We now consider the limit: $n = \alpha/\gamma$, $p = x\alpha/\gamma$, $\gamma \to 0$, where α is a constant of proportionality and $x \in [-1, 1]$. We have

$$\lim_{\gamma\to 0} \sqrt{\frac{1-x^2}{1-2k\gamma/\alpha + k^2\gamma^2/\alpha^2 - x^2}} \left(\frac{(1+x)\alpha}{(1+x)\alpha - k\gamma}\right)^{(1+x)\alpha/\gamma} \times \left(\frac{(1-x)\alpha}{(1-x)\alpha - k\gamma}\right)^{(1-x)\alpha/\gamma} \left(\frac{\alpha^2 - 2\alpha k\gamma + k^2\gamma^2 - x^2\alpha^2}{e^2\gamma^2}\right)^k$$

To first order around $y = 0$, $\frac{\beta}{\beta - ky}^{\beta/y} = e^k \ \forall \ \beta \in \mathbb{R}$. Taking the limits and recombining, we obtain the final expression

$$I_H(p) \approx \left[(-1)\sin\gamma\cos^{2n}\gamma \sum_{k=0}^{n-|p|} \left((-1)^k \tan^{2k}\gamma\right)\left(n^2 - p^2\right)^k\right]^2 \tag{2.53}$$

From the definition of the ordinary Bessel functions $\mathrm{J}_\alpha = \sum_{m=0}^{\infty} \frac{-1^m}{m!\Gamma(m+\alpha+1)}(x/2)^{2m+\alpha}$, we can see from 2.53 that for suitably large n

$$I_H(p) \approx \left[-\sin\gamma\cos^{2n}\gamma \mathrm{J}_0(2n\tan\gamma\sqrt{1-p^2/n^2})\right]^2 \approx \gamma^2 \mathrm{J}_0^2(2n\gamma\sqrt{1-p^2/n^2}) \tag{2.54}$$

Which is analogous to the spherical wave solution to the T-T equations given in Eq. 2.29

For the transmitted beam, notice that at every point except $p = a$, there are no paths of 0 reflections. Therefore, under the condition that $p \neq a$ we can run the sum starting at $n = 1$. Like in the reflected beam case, we consider the limit where $\gamma \to 0$ while $\gamma \cdot n$ and $\gamma \cdot p$ are kept constant like $n = \alpha/\gamma$ and $p = x\alpha/\gamma$. Applying the binomial identity $\binom{n}{k} = \frac{n}{k}\binom{n-1}{k-1}$, and expanding:

$$\Psi(p) = \sum_{k=1}^{n-|p|} (-1)^k \gamma^{2k} \binom{n-p-1}{k-1}\binom{n+p+1}{k} \tag{2.55}$$

$$= \sum_{k=1}^{n-|p|} (-1)^k \gamma^{2k} \frac{n+p+1}{n-p}\binom{n-p}{k}\binom{n+p}{k-1} \tag{2.56}$$

$$= \sum_{k=1}^{n-|p|} (-1)^k \gamma^{2k} \frac{n+p+1}{n-p} \frac{(n-p)!(n+p)!}{k!(k-1)!(n-p-k)!(n+p-k+1)!} \tag{2.57}$$

We apply Stirling's approximation, $n! = \sqrt{2\pi n}(n/e)^n$, as well as the appropriate limits

$$\begin{aligned}
\Psi_0(p) &= \sum_{k=1}^{n-|p|}(-1)^k\gamma^{2k}\frac{1}{k!(k-1)!}\frac{n+p+1}{n-p}\sqrt{\frac{n^2-p^2}{(n-p-k)(n+p+1-k)}}\left(\frac{n-p}{e}\right)^{n-p}\times \\
&\left(\frac{n+p}{e}\right)^{n+p}\left(\frac{n-p-k}{e}\right)^{-(n-p-k)}\left(\frac{n+p-k+1}{e}\right)^{-(n+p-k+1)} \\
&= \sum_{k=1}^{n-|p|}(-1)^k\gamma^{2k}\frac{1}{k!(k-1)!}\frac{\alpha(1+x)+\gamma}{\alpha(1-x)}\sqrt{\frac{\alpha^2(1-x^2)}{(\alpha(1-x)-k\gamma)(\alpha(1+x)+(1-k)\gamma)}}\times \\
&\left(\frac{1-x}{1-x-k\gamma}\right)^{(\alpha/\gamma(1-x))}\left(\frac{1-x}{1-x-k\gamma}\right)^{(\alpha/\gamma(1-x))}\times \\
&\left(\frac{\alpha(1-x)/\gamma-k}{e}\right)^{k}\left(\frac{\alpha(1+x)/\gamma-k+1}{e}\right)^{k-1}
\end{aligned}$$

Like in the reflected case, consider the fact that to first order around $y=0$, $\frac{\beta}{\beta-ky}^{\beta/y} = e^k \;\forall\; \beta \in \mathbb{R}$. We obtain

$$\begin{aligned}
\Psi_0(p) &= \sum_{k=1}^{n-|p|}(-1)^k\gamma^{2k}\frac{1}{k!(k-1)!}\frac{\alpha(1+x)+\gamma}{\alpha(1-x)}e^k e^{k-1}\times \\
&\left(\frac{\alpha(1-x)/\gamma-k}{e}\right)^{k}\left(\frac{\alpha(1+x)/\gamma-k+1}{e}\right)^{k-1} \\
&= \sum_{k=1}^{n-|p|}(-1)^k\gamma^{2k}\frac{1}{k!(k-1)!}\frac{\alpha(1+x)+\gamma}{\alpha(1-x)}\left(\alpha(1-x)/\gamma-k\right)^{k}\left(\alpha(1+x)/\gamma-k+1\right)^{k-1} \\
&= \sum_{k=0}^{\infty}(-1)^{k+1}\gamma^{2k+2}\frac{1}{k!(k+1)!}\frac{n+p}{n-p}(n-p)^{k+1}(n+p)^k \\
&= \sum_{k=0}^{\infty}(-1)^{k+1}\gamma^{2k+2}\frac{1}{k!(k+1)!}(n+p)(n^2-p^2)^k
\end{aligned}$$

$$
\begin{aligned}
&= \sum_{k=0}^{\infty} (-1)^{k+1} \gamma^{2k+2} \frac{1}{k!(k+1)!} \sqrt{(n+p)^2} (n^2 - p^2)^k \\
&= \sum_{k=0}^{\infty} (-1)^{k+1} \gamma^{2k+2} \frac{1}{k!(k+1)!} \sqrt{\frac{(n+p)(n+p)(n-p)}{(n-p)}} (n^2 - p^2)^k \\
&= \sum_{k=0}^{\infty} (-1)^{k+1} \gamma^{2k+2} \frac{1}{k!(k+1)!} \sqrt{\frac{n+p}{n-p}} \sqrt{n^2 - p^2} (n^2 - p^2)^k \\
&= -\gamma \sqrt{\frac{n+p}{n-p}} \sum_{k=0}^{\infty} \frac{(-1)^k}{k!(k+1)!} (n\gamma \sqrt{1 - p^2/n^2})^{2k+1}
\end{aligned}
$$

From the definition of the ordinary Bessel functions, $\mathrm{J}_\alpha = \sum_{m=0}^{\infty} \frac{-1^m}{m!\Gamma(m+\alpha+1)} (x/2)^{2m+\alpha}$, we obtain that the intensity across the face of the crystal is

$$
I_0(p) = |\Psi(p)|^2 = \gamma^2 \frac{n+p}{n-p} \mathrm{J}_1(2n\gamma \sqrt{1 - p^n/n^2})^2
$$

In summary, the intensities $I_{0,H} = \psi_{0,H} \psi_{0,H}^*$ take the form

$$
I_H(p) = \gamma^2 \mathrm{J}_0^2(2n\gamma \sqrt{1 - p^2/n^2}) \tag{2.58}
$$

$$
I_0(p) = \gamma^2 \frac{n+p}{n-p} \mathrm{J}_1^2(2n\gamma \sqrt{1 - p^2/n^2}) \tag{2.59}
$$

Comparing Eqs. 2.58 and 2.59 to Eqs. 2.29 and 2.30 we can note that they are equivalent when we set $\Gamma = p/n$ (from its definition), $|A_0^2| = 1$ and $n \cdot \gamma = (\pi/2)\frac{D}{\Delta_H}$, as expected from equation 2.33.

2.2.3 Determining simulation parameters from experimental variables

Since γ and the number of simulation bi-layers n are related to the crystal parameters by

$$
n \cdot \gamma = \pi/2 \frac{D}{\Delta_H} \tag{2.60}
$$

there is a degree of freedom when choosing the parameters when simulating a given experiment. One can sacrifice accuracy for speed by decreasing the number of layers n, as long as γ is adjusted such that the relation in Eq. 2.60 is maintained. Changing γ changes

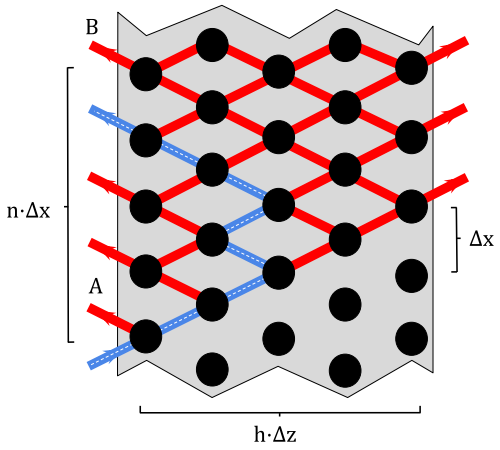

Figure 2.3: A lattice as it is used in the model in the Bragg case. The nodes in the lattice are functionally identical to the one presented in Fig. 2.2b. The reflected intensity at node n is a sum of the contributions from all the paths which leave the crystal from the edge at node n. The widths Δx, Δz once again correspond to the lattice spacing in simulations. The height of the neutron paths through the crystal cannot exceed height h, which corresponds to the crystal thickness in simulation space. Illustrated in blue (dashed) is a Dyck path of length 6, bound by height 2 and containing 2 peaks. The points A and B correspond to the points of geometric reflection from the front and back face of the crystal, respectively, where the reflected intensity is typically the highest. Previously published in [1].

the resolution of the simulation, and as $\gamma \to \pi/2$ the intensity profiles become coarser. In this scenario, the QI model does not provide sufficient accuracy to capture small scale oscillations. Conversely, the exactness of the model output increases as $\gamma \to 0$ and $n \to \infty$, and results are already an excellent match to Eqs. 2.58 and 2.59 when γ is on the order of $\pi/100$. In this case, a crystal with a Pendellösung thickness D/Δ_H of 100 would be composed of 5000 lattice columns, which corresponds to 10000 (10000x10000) sparse matrix multiplications which is a simple task for a modern computer. The simulation output must also be interpreted differently depending on the choice of parameters. The effective size of a simulation layer depends on the crystal thickness D, as well as the number of bi-layers n

$$\Delta x \cdot n = D \tag{2.61}$$

and the lattice spacings in both axes are related through the Bragg angle

$$\frac{\Delta z}{\Delta x} = \tan \theta_B \tag{2.62}$$

Since the simulated intensity is specified at each node, the spatial coordinate must be scaled by a factor of Δz. By substituting the definition of Δ_H into Eq.2.60, we obtain an expression for γ and Δx in terms of crystal characteristics

$$\frac{\gamma}{\Delta x} = \frac{d|F_H|}{V_{cell}} \tag{2.63}$$

where d is the distance between Bragg planes and V_{cell} is the volume of a unit cell in the crystal. From this expression, we can observe that in the small γ limit, variations in the value of γ are analogous to variations in the Bragg plane distance inside the crystal, such as those resulting from strains or deformations. These effects are a computational challenge in the standard theory of dynamic diffraction, while this model offers an approach to solve these problems without the need for complex calculations. Depending on one's choices for the model parameters, the simulated profiles can often be produced very quickly, with high accuracy, and without the need for complex analytical calculations. It must be noted that these equivalences are independent of any assumption about the material, other than that it induces dynamical diffraction. The simulation nodes must be thought of as theoretical diffraction sites inside the crystal, whose separation depends on the choice of γ and ranges between the size of one crystal unit cell to one Pendellösung length. The angle between the nodes is set by the Bragg angle. The dependence on the structure factor F_H accounts for differences in the crystal structure, and thus the model is not limited to a specific atom arrangement in the unit cell.

2.2.4 QI Model, Bragg Case

To extend the model to the Bragg case, we introduce empty nodes, consisting of the "transmission matrix"

$$T = \begin{pmatrix} 1 & 0 \\ 0 & 0 \\ 0 & 0 \\ 0 & 1 \end{pmatrix} \tag{2.64}$$

to create regions of the simulation environment where the neutron is propagating through empty space. It then becomes possible to simulate Bragg diffraction by filling only a segment of the simulation space with crystal nodes, and the rest with empty space in which we place a detector to keep track of the intensity being reflected from the crystal. More generally, any node can be removed by replacing the appropriate block in one of the column matrices C (Eq. 2.41) by the matrix T to simulate a crystal sample of any shape. The nodes can also be modified individually to model the presence of strains or defects.

To demonstrate that the parameter definitions are consistent between the Laue and Bragg geometries, we would like to obtain an analytical expression for the reflected intensity in the Bragg case like we did for the Laue case. Since the neutron never re-enters the crystal after leaving it, we can see that this problem is equivalent to counting the number of Dyck paths [64] with some length n, a fixed number of peaks k and a maximal height h. A Dyck path is a lattice walk starting at $(0, 0)$ which only allows movements of $(+1, +1)$ and $(+1, -1)$, and never drops below the x axis. In Fig. 2.3, we illustrate in blue that a path through a lattice in the Bragg geometry is equivalent to a Dyck path.

The total number of Dyck paths of length $2n$ is given by the Catalan numbers

$$C_n = \frac{1}{n+1}\binom{2n}{n}. \tag{2.65}$$

However, similar to the Laue case, the weight associated with each path depends on the number of reflections which it has undergone. Because the paths must leave from the same face through which they entered, the number of reflections is always odd and we can simply count the number of peaks k of each path, defined as a local maximum in path height. The number of Dyck paths of length $2n$ with exactly k peaks is given by

$$N(n, k) = \frac{1}{n}\binom{n}{k}\binom{n}{k-1} \tag{2.66}$$

which correspond to the Narayana numbers. If the crystal thickness was infinite, this would be enough to derive an expression for the reflected intensity everywhere. However, in the

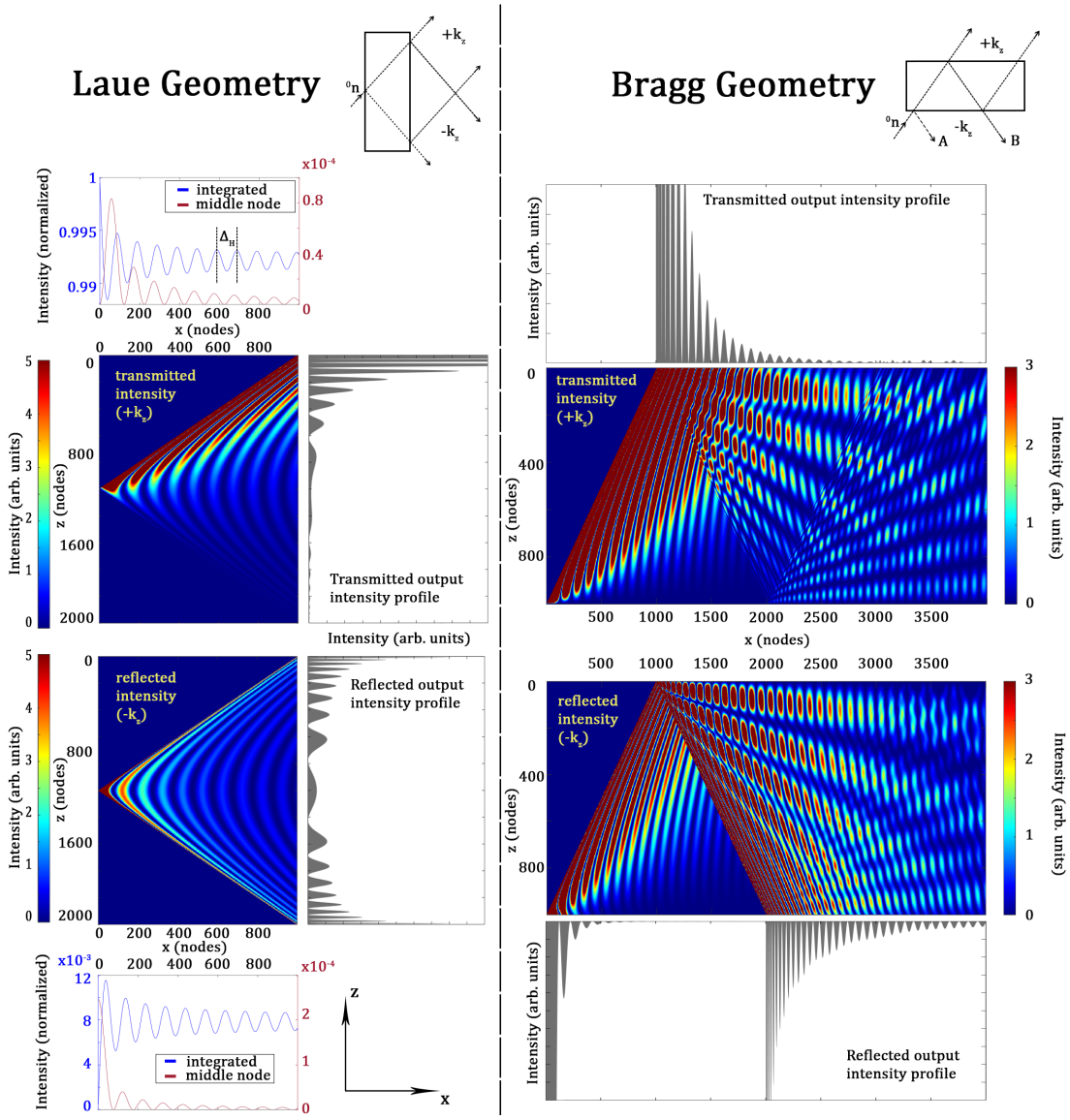

Figure 2.4: The intensity distributions inside the crystal for the Laue case (left) and Bragg case (right). The top row figures are for the transmitted path (post selected on $+k_z$ momentum) and the bottom row figures are for the reflected path (post selected on $-k_z$ momentum). For each case we plot the output intensity profiles corresponding to the intensity at the end nodes. Lastly, the integrated intensities for the Laue case are plotted under the crystal figures showing the Pendellösung oscillations with period Δ_H. Previously published in [1]. © 2022 American Physical Society

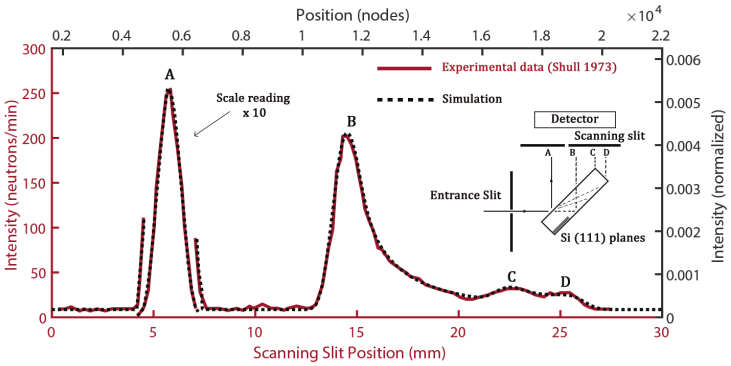

Figure 2.5: In red, full line: A Bragg-reflected intensity distribution measured at the exit face of a crystal by use of a scanning slit, from [2]. In black, dotted line: A simulated intensity profile in the Bragg case, where we have chosen the parameters according to Eqn. 2.60 and Shull's experimental parameters. The simulation output was convolved with the shape of the A peak to account for experimental effects such as slit width and beam momentum distribution. The points A, B, C and D correspond to the geometric reflection points as shown in the inset diagram. Previously published in [1]. © 2022 American Physical Society

finite crystal case, starting at $n = h$, some of the fewer-peaked paths will leave the crystal through the top edge. These paths generally have a higher weight in the small γ limit due to the factor of $\sin\gamma$ introduced on a reflection, and therefore cannot be neglected. For a complete description, we require an expression for the number of Dyck paths of length $2n$, with exactly k peaks and which are bound above by height h, which we will denote $H(n, k, h)$. Unfortunately, there is no known closed form for these numbers, but it is possible to derive a recursion relation which allows for any one of them to be computed. We divide a path from $(0, 0)$ to $(2n + 2, 0)$ into two sections, from 0 to $2i$ and $2i$ to $2n + 2$, where $(2i, 0)$ is the last point at which the path returns to the x axis before it ends. There are n possibilities for i, where $i = 0$ means the path does not return to the x axis between the first and last point. There are $\sum_{j=0}^{i} H(i, j, h)$ such possible paths. After the path touches the x axis at $x = 2i$, the next movement is necessarily upwards, and the final movement from $(2n, 1)$ to $(2n + 2, 0)$ is necessarily downwards. Furthermore, this second path will never touch the x axis again, and will never go above height h: we can therefore describe it as a path of half-length $n - i$ and bounded by height $h - 1$. Because the number of peaks of both halves must add up to k, and there are n choices for i, the total number

of paths $H(n+1,k,h)$ is given by

$$H(n+1,k,h+1) = \sum_{i=0}^{n}\sum_{j=0}^{i} H(i,j,h)H(n-i,k-j,h-1) \tag{2.67}$$

With initial conditions

- $H(0,k,h) = \delta_{k0}$
- $H(n,0,h) = \delta_{n0}$
- $H(n,k,0) = \delta_{n0}\delta_{k0}$

Using the aforementioned Narayana numbers and the same definitions as in the Laue case, we can find the reflected amplitude inside the AB region (Fig. 2.3) where it is unaffected by reflections off of the back face of the crystal

$$\psi_H(n) = \sum_{k=1}^{n}(-1)^{k-1}\sin^{2k-1}\gamma\cos^{2(n-k+1)}\gamma\frac{1}{n}\binom{n}{k}\binom{n}{k-1} \tag{2.68}$$

Once again, we consider the limiting case $\gamma \to 0$ with $\gamma \cdot n$ kept constant. Here, we find the that reflected intensity is of the form

$$I_H(n) = \frac{1}{n^2}\mathrm{J}_1^2(2\gamma n) \tag{2.69}$$

Note that in this geometry, n being the path length corresponds to the position variable on the detector. Consequently, we now define h as number of nodes in the direction of the Bragg planes. It has been shown experimentally that there is a secondary reflection peak on the point of geometrical reflection $n = h$. However, the intensity for $n < h$ is independent of h since the outgoing paths have not yet had the chance to reach the top of the crystal. In this sense, equation 2.69 is a good match for experimental data when simply looking at the primary reflection peak. Furthermore, it is equivalent to the analytical solution found in [65] for the same region.

Although we do not have a general analytical expression for the intensity in the Bragg case, we are still able to obtain an intensity profile for any shape through numerical computation. The similarities and differences of dynamical diffraction in the Laue case and Bragg case can be contrasted by examining the intensity inside the crystals. Fig. 2.4 shows

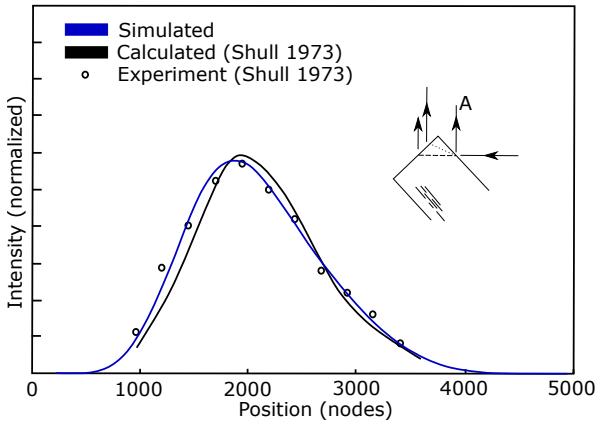

Figure 2.6: In black, full line: The neutron intensity profile reflected from the corner of a Bragg crystal, from [2]. The profile calculated by Shull is displayed as a full black line, and the corresponding experimental data points are showed. In blue, full line: The QI model simulation where the parameters were varied to obtain a good match with the experimental data. The output intensity profile was convoluted with the same profile as in Fig. 2.5. Previously published in [1]. © 2022 American Physical Society

the intensities inside the crystal on the transmitted path or the reflected path. One can observe the oscillation pattern inside the crystal that leads to the Pendellösung oscillations as well as the output intensity profiles corresponding to the intensity at the last node.

The diffracted neutron intensity in the Bragg case was measured by C.G. Shull and colleagues [2] using a scanning slit to determine the beam profile exiting a crystal. In DD theory the Bragg case has 100 % reflectivity for neutrons falling within a narrow angular range called the Darwin width

$$\theta_D = \frac{\lambda^2 |F_H|}{\pi V_{\text{cell}} \sin^2(2\theta_B)} \tag{2.70}$$

which is typically on the order of an arcsecond. Neutrons outside this range propagate through the crystal and can reflect off the back face ultimately exiting from the front. Those neutrons exiting the crystal in this way are spatially displaced from the primary diffraction peak by an amount $2t/\tan(\theta_B)$. In Ref. [2], neutrons ($\lambda = 4.43$ Å) were directed at a silicon crystal with $\theta_B = 44.9°$. The results from [2] are shown in Fig. 2.5. The primary peak (labeled A) was measured to have approximately 10 times the intensity of the secondary peak (labeled B). Two additional small peaks were observed in locations corresponding to neutrons exiting the corners of the crystal.

In the same figure, we have overlaid the output of our simulation model (dashed black curve). The model parameters such as γ and the number of nodes were calculated from the experimental parameters found in Ref. [2] using the relationship presented in equation 2.60 and by setting γ to $\frac{\pi}{50}$. The model is able to accurately simulate the features observed in the experimental intensity, such as the presence of a primary peak at the first geometrical reflection point, as well smaller secondary peaks which appear where the neutron has reflected off of the back face and corners of the crystal. To obtain a proper intensity profile from the simulations, it is necessary to account for the shape of the incoming beam. This can be accomplished by convolving the simulation output with the experimentally obtained shape of the first (A) peak. The points were sampled from the original figure using the GetData graph digitizer tool, and were convolved with the simulation output in MATLAB. The QI model enables one to easily vary the geometry of the crystal that is being analyzed. It is possible to vary the angle of the CD side of the crystal in the simulations. By performing a least-squares fit, it is found that good agreement is obtained when the CD side of the crystal is at an angle of $91.35° \pm 0.07°$ relative to the AC side. The QI model can also be applied to simulate the data from the corner of a Bragg crystal as shown in Fig. 17 of Ref. [2]. The same crystal geometry/parameters (including the 91.35° corner angle) and beam characteristics as that of our Fig. 2.5 were used. Here it was required to estimate for the physical location of the beam entrance point with respect to the corner of the crystal (the "m/c" parameter) as it was not specified in Ref [2]. We find good agreement when the beam is set to enter the crystal 6.2 mm away from the corner point. The results displayed in Fig. 2.6 once again demonstrate that the model is a good match for experimental data in the mixed Laue-Bragg case.

2.2.5 QI Model, Neutron Cavity

Modelling of a Neutron Cavity

The work in this section has been previously presented in [3].

Dynamic diffraction theory predicts that in the Bragg geometry, neutrons falling within a narrow range of momentum centered around the Bragg condition (the Darwin width) are reflected with close to 100% probability. In a neutron cavity composed of two perfect crystals, neutrons outside the Darwin width will escape through the crystals within the first few bounces. Conversely, neutrons inside this width are effectively confined, allowing for a great number of bounces. Interestingly, the QI model predicts that this result can be explained purely as a consequence of a quantum random walk: the total neutron wave-function is expressed as a sum over all the possible paths through the Bragg lattice. The

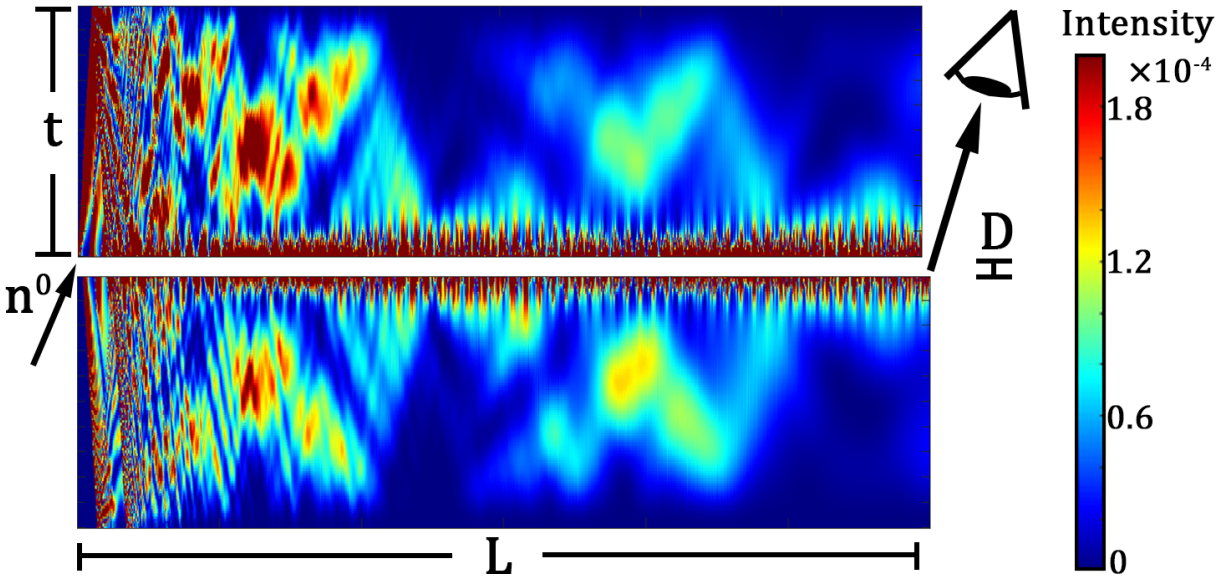

Figure 2.7: The simulated neutron intensity inside two perfect-crystal silicon blades acting as a neutron cavity. The neutron is initialized as an incident spherical wave to the corner of the top crystal. Given that most of the beam gets initially transmitted, the range of the color bar is limited to emphasize the confined intensity. The crystals are placed a distance D apart, have thickness t and length L. After the first few bounces, most of the leftover neutron intensity is contained within a small band on the inside edges of the crystals. This intensity is preserved with further propagation. A detector can be placed at the exit of the crystals to capture the neutrons exiting the cavity. This simulation ($\Delta_H \approx 50\mu$m, $t \approx 0.5$mm, $D \approx 0.2$mm, $L \approx 3$cm) considers a very thin crystal slice to better illustrate the behavior near the gap. Previously published in [3].

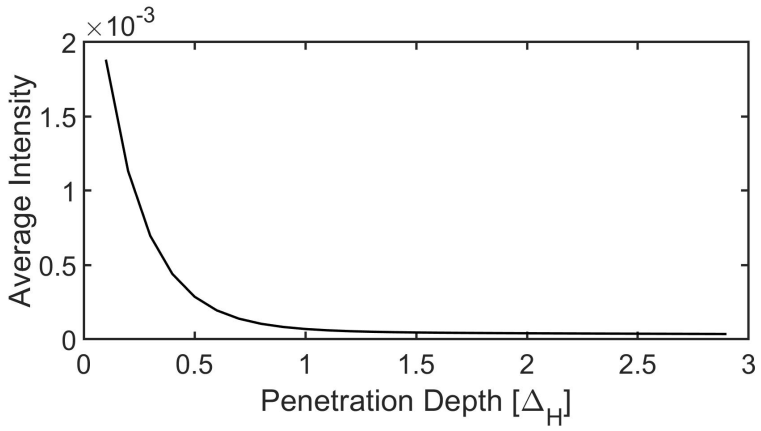

Figure 2.8: The average neutron intensity across a horizontal slice of the top crystal shown in Fig. 2.7 is plotted as a function of the penetration depth inside the top crystal. The intensity drops sharply within the first Pendellösung period, indicating that the neutron is confined within a band of width $\approx \Delta_H$ inside the cavity. Previously published in [3].

difference in phase accumulated by the different paths results in constructive interference only for the paths which stay confined in a small region close to the gap.

As shown in Fig. 2.7, without any information about transverse momentum, boundary conditions, or incident angle, the model predicts that only after a few bounces, the intensity is almost entirely localized in a narrow band around the inter-crystal gap. Most neutrons that do not settle within this band are either transmitted straight through the top of the crystal interferometer, or bounce at most once and transmit through the bottom.

Shown in Fig. 2.8 is the neutron average intensity across a horizontal slice of the top crystal as a function of penetration depth into the top crystal. The intensity drops sharply within the first Δ_H, showing that the neutron does not penetrate very deeply inside the crystal after a few bounces.

Confined Intensity

With the QI model we can examine the neutrons which remain confined within the cavity. Fig. 2.9 a) shows the confined intensity inside the cavity as a function of the number of bounces, for cavity parameters $D = 12\Delta_H$ and $t = 87.5\Delta_H$. It is to be noted that as the neutron progresses through the cavity, the individual bounces become hard to resolve, and therefore here we are considering a length of crystal corresponding to a geometrical path of

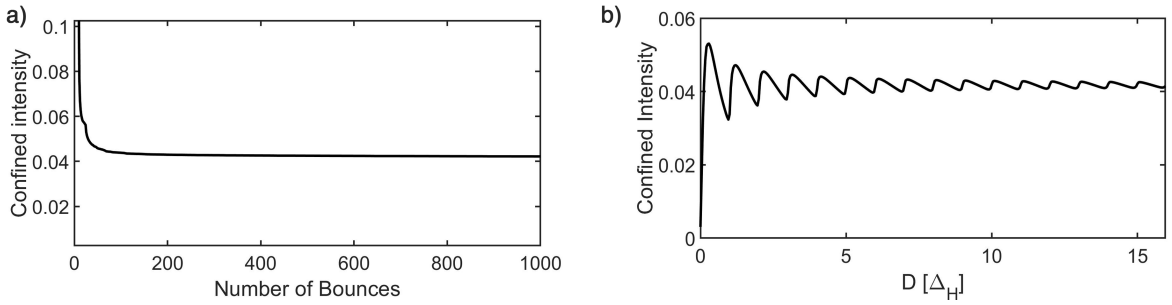

Figure 2.9: a) The neutron intensity remaining inside the cavity as a function of the number of bounces, for a cavity with $D = 12\Delta_H$ and $t = 87.5\Delta_H$. The intensity drops very sharply during the first few bounces then stabilizes as the direct beam leaves the top crystal. A value for the reflectivity of the crystal of $\approx 1 - 1.6 \times 10^{-5}$ was extracted by fitting to an inverse exponential between bounces 500 and 800. b) The neutron intensity remaining inside the cavity after a length of 16000 Δ_H. The neutron undergoes a number of bounces proportional to D^{-1}. The final intensity in the cavity oscillates with period $D = \Delta_H$. Previously published in [3].

1000 bounces. The intensity drops sharply as the direct beam transmits straight through the first crystal, and then drops slightly less at each subsequent reflection. Eventually, it settles to an effectively constant value of around 4 % of the incoming intensity. An estimation for the reflectivity of the crystal as the number of bounces increases can be extracted from this curve, by fitting it to an inverse exponential. The reflectivity in the "stable" region between 500 and 800 bounces is found to be $(\approx 1 - 1.6 \times 10^{-5})$, as shown in Fig. 2.10.

In Fig. 2.9b, the intensity remaining in the cavity after a length $L = 16000\Delta_H$ is plotted as a function of D. The confined intensity oscillates with period $D = \Delta_H$. The QI model indicates that to maximize the number of bounces for a given set of crystals, the spacing can be made very small without losing much intensity at the exit, but should be made no smaller than $\Delta_H/4$.

Cavity Modes

Simulation of the neutron cavity using the QI model shows that the neutrons inside the cavity settle in one of two regimes, depending on the intercrystal distance D. It should be noted that in the limit where $D \to 0$, the system reduces to a simple Laue crystal of thickness L, in which case the neutron will diverge to the edges of the Bormann triangle

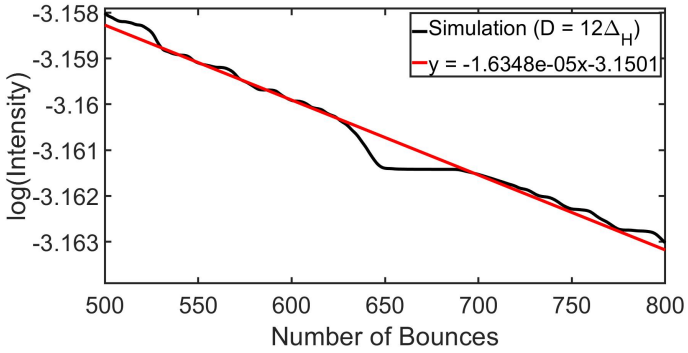

Figure 2.10: The reflectivity of the neutron cavity extracted from the plot in Fig. 2.9a. A straight line is fitted through the log space plot of the intensity. For an expected dependence of $I(N) = I_0 R^N$ (where N is the number of bounces), $\log(I) = \log(I_0) + N\log(R)$ and the reflectivity is given as the exponential of the slope of the fitted line. For $\log(R) \approx 0$, $e^{\log(R)} = R \approx 1 + \log(R)$. Previously published in [3].

as predicted by DD theory. However, for nonzero spacing, after the first few bounces, most of the neutron current is confined within a small band of size of order Δ_H on the inside surface of the cavity, and bounces back and forth without penetrating very deeply into the crystal. Fig. 2.11a shows the simulated reflected intensity on the surface of the top crystal throughout the cavity, for different values of D. For the D $< \Delta_H$ regime, the neutron behaves like a standing wave inside the cavity, with a period dependant on D. For the regime with larger values of D ($> 2\Delta_H$), the bounces are well-separated and localized at first. As the number of bounces increases, the neutron wave packets spread and induce interference effects. This behavior is shown in Fig. 2.11b: for small D, there is one dominant frequency which changes with D. As D increases, more pairs of harmonics are introduced.

Experimental Implementation

An experimental implementation of a neutron cavity was performed at the NIOF beamline at the National Institute of Standards and Technology (NIST) center for neutron research (NCNR). The setup is shown in Fig. 2.12. A beam of neutrons with wavelength 0.235 nm was propagated through a 10 mm wide silicon neutron cavity composed of two 10 mm thick perfect-crystal silicon blades (220 reflection) attached to a common base. The theoretical pendellösung length for this configuration is found to be 50.38 μm. The neutrons

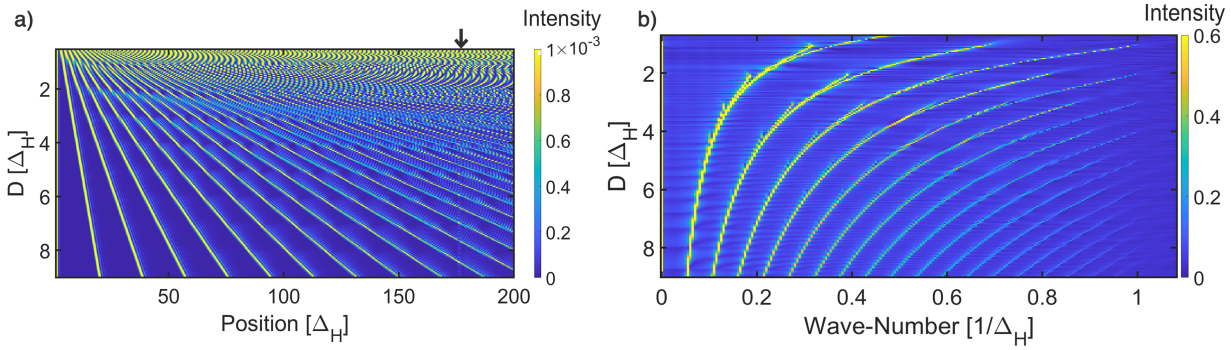

Figure 2.11: a) The intensity reflected from the bottom surface of the top crystal as a function of position, for different intercrystal spacing distances D. There are two different regimes: when the spacing is smaller than the pendellösung length, the neutron state is represented by a standing wave, whose frequency depends on crystal spacing. The second regime is where the spacing is larger than the pendellösung length. Here the neutron bounces are well-separated at first followed by self interference after many bounces. There is a noticeable disruption around 175 Δ_H (indicated by an downwards arrow) caused by the first reflection from the back face of the top crystal. b) The frequency spectrum of the intensity profiles shown in Fig. 2.11a. In the region of $D < \Delta_H$, there is one dominant frequency, which varies with D. As the spacing increases, the neutron bounces become well-separated, and new frequencies appear corresponding to the higher harmonics of the main bounce frequency. Previously published in [3].

underwent four well-defined bounces before leaving the cavity at the exit. A scanning slit and an integrating detector were placed behind the top crystal, and were used to map the spatial intensity of neutrons along the crystal cavity.

Using the QI model we can simulate the experimental configuration. The simulation parameters were chosen according to the equivalence relation of Eq. 2.60. As shown in Ref. [1] we can account for the experimental factors such as the spread of the incident beam, beam divergence, and slit size through the analysis of a Bragg diffraction peak. Similar to the methods of Ref. [1] the intensity penetrating through the top crystal was convolved with the measured shape of the exit peak. The simulated intensity throughout the setup is shown as a false-color map, and the simulated integrated intensity at the detector is shown above the setup in a black, dashed line. The simulated intensity profile is in good agreement with the measured intensity profile. It can be observed that the majority of the contribution to the exiting beam of the cavity comes from the classical bouncing path.

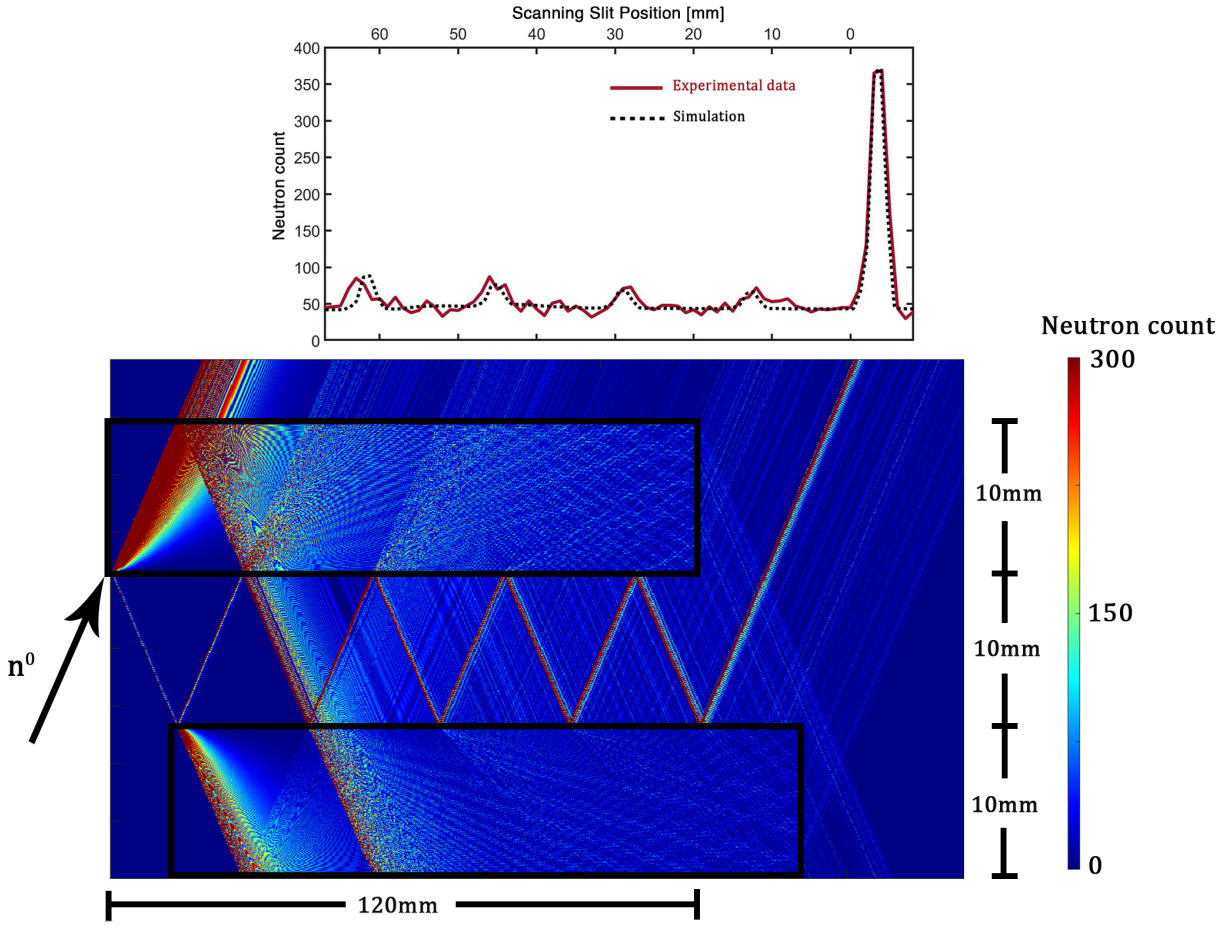

Figure 2.12: The experimental implementation of a neutron cavity using two perfect-crystal silicon blades and a position sensitive neutron detector above the top blade. Using the described QI model of DD we can simulate the neutron propagation through the cavity. Here the nodes outside the two crystals act as identity matrices, while a quantum random walk occurs inside the two crystals. No further physics or boundary conditions are present. The geometric trajectory of the neutron as it bounces back and forth is clearly visible between the two crystals. Shown above in red is the experimental measurement corresponding to this geometry. Overlaid in the black, dashed line, is the intensity obtained via the QI model. Note that as shown in Ref. [1], the QI model accounts for experimental parameters by convolving the intensity output with the shape of the exiting beam. Good agreement is found between the simulation and experiment. Previously published in [3].

2.3 Conclusions

In this chapter, we have demonstrated that dynamical diffraction effects for particle diffraction in perfect crystals can be modeled in general with the help of quantum random walks. We have applied this model to the basic cases of the Laue and Bragg geometries, where it produces consistent results with established theory. In more complicated geometries such as in a mixed Laue/Bragg corner, the results are consistent with experiments when accounting for external factors such as beam divergence. Since the individual nodes in the lattice can be edited without adding much to the computational complexity, the model is a good candidate for modeling crystal "imperfections" such as defects, strains, or dislocations. It is our hope that this model will be useful in the future to design new, more precise neutron optical elements for use in, for example, neutron interferometry experiments.

Chapter 3

Neutron Whispering Gallery

3.1 Theory

In 2009, it was suggested by Nesvizhevsky *et al.* [66] that by diffracting a neutron along the edge of a curved crystal, one could observe quantum states similar to those found in a gravitational potential. These states have been observed experimentally, and have promising applications in neutron physics. In this section, I will briefly describe the theory behind these centrifugal states, as well as how simulations can help with the design of future experiments.

In a curved system such as in Fig. 3.1, the potential as experienced by the neutron can be expressed in terms of the optical potential of the mirror, as well as the potential resulting from the centrifugal acceleration of the curved path. A critical assumption which must be made is that the variations in ρ of the neutron within the crystal are small compared to R, and such the centrifugal acceleration can be approximated as v^2/R.

To derive the wavefunction of the neutron inside the mirror, we begin by setting up the Schrödinger equation in cylindrical coordinates:

$$\left[-\frac{\hbar^2}{2M}\left(\frac{\partial^2}{\partial\rho^2}+\frac{1}{\rho}\frac{\partial}{\partial\rho}\right)-\frac{\hbar^2}{2M\rho^2}\frac{\partial^2}{\partial\phi^2}+U(\rho)-E\right]\psi(\rho,\phi)=0 \tag{3.1}$$

where M is the mass of the neutron, and the optical potential $U(\rho)$ can be described as a step function

$$U(\rho)=-U_0\Theta(R-\rho)=\begin{cases}-U_0, & \rho\leq R\\ 0 & \rho>R\end{cases} \tag{3.2}$$

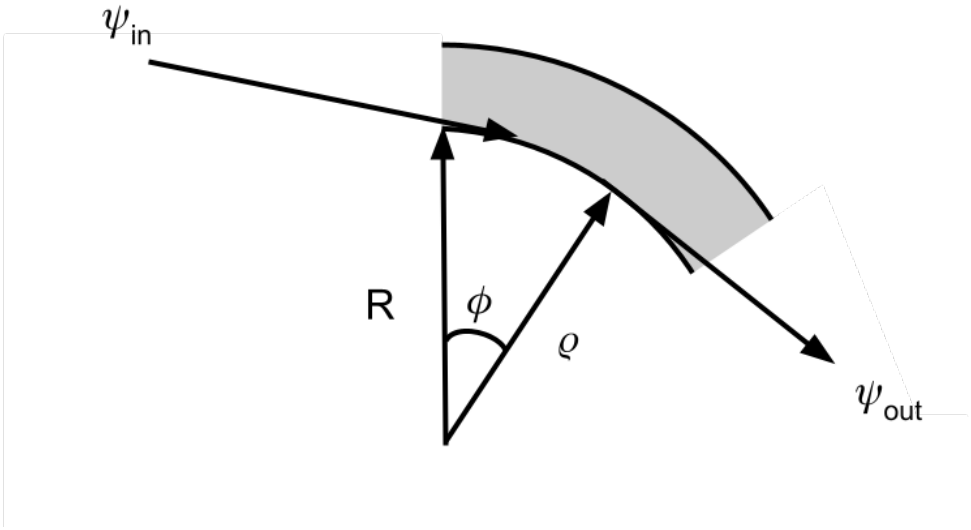

Figure 3.1: Schematic representation of a neutron whispering gallery experiment. A neutron in state ψ_{in} enters a curved crystal at an angle almost tangential to the inner surface. The neutron settles in a superposition of quasi-stationary states inside the crystal before exiting in states ψ_{out}. R is the radius of curvature of the mirror, ρ and ϕ are radial and angular coordinates.

We now make the standard substitution $\psi(\rho,\phi) = \Phi(\rho,\phi)/\sqrt{\rho}$, and expand into the angular momentum state eigenbasis:

$$\Phi(\rho,\phi) = \sum_{\mu=-\inf}^{\inf} \chi_{|\mu|(\rho)e^{i\mu\phi}} \tag{3.3}$$

The number μ determines the angular momentum of the state in units of $\hbar$. Equation 3.1 becomes

$$\left[-\frac{\hbar^2}{2M}\left(\frac{\partial^2}{\partial\rho^2}\right) + \frac{\hbar^2}{2M\rho^2}\left(\mu^2 - \frac{1}{4}\right) - U_0\Theta(R-\rho) - E\right]\chi_\mu(\rho) = 0 \tag{3.4}$$

Introducing the parameter $z = \rho - R$ and expanding the centrifugal energy to first order around $z = 0$:

$$\left[-\frac{\hbar^2}{2M}\frac{\partial^2}{\partial z^2} + \hbar^2\frac{\mu^2 - 1/4}{2MR^2}\left(1 - \frac{2z}{R}\right) - U_0\Theta(-z) - E\right]\chi_\mu(z) = 0 \tag{3.5}$$

The solution to Eq. 3.5 can be expressed in terms of the Airy functions. More specifically, we must impose that the scattered waves be everywhere outgoing, which corresponds to the boundary condition that the state asymptotically behaves like the Green function for the total Hamiltonian [67]. The states χ_μ are then expressed as:

$$\chi_\mu(z) = \begin{cases} D_\mu(\mathrm{Bi}(z_0 - z/l_0 - \epsilon_\mu/\epsilon_0) + i\mathrm{Ai}(z_0 - z/l_0 - \epsilon_\mu/\epsilon_0)), & z > 0 \\ \mathrm{Ai}(-z/l_0 - \epsilon_\mu/\epsilon_0), & z \leq 0 \end{cases} \tag{3.6}$$

where

$$l_0 = (\hbar^2 R/(2M^2v^2))^{1/3} \tag{3.7}$$

has units of length and can be considered as the characteristic length scale,

$$\epsilon_0 = (\hbar^2 M v^4/(2R^2))^{1/3} \tag{3.8}$$

has units of energy, $z_0 = \epsilon_0/U_0$ and

$$\epsilon_\mu = \lambda_\mu \epsilon_0 \tag{3.9}$$

corresponds to the radial kinetic energy of the state. The constants D_μ ensure that the wavefunction is continuous at the miror boundary, and are given by

$$D_\mu = \frac{Ai(-\lambda_\mu)}{Bi(z_0 - \lambda_\mu) + iAi(z_0 - \lambda_\mu)} \tag{3.10}$$

and the constants λ_μ are found . These states are called quasi-stationary states, due to their relative stability which depends on the neutron centrifugal energy. The states with high centrifugal energy tunnel into the mirror with high probability, and thus have low lifetimes and are unlikely to be detected at the output. The deeply bound states with low energy have very long lifetimes and contribute most of the intensity observed on the detector.

Before expressing the full state of the neutron as a sum of quasistationary states, they must be normalized

$$\chi_\mu = C_\mu \chi'_\mu \tag{3.11}$$

where

$$\frac{1}{C_\mu} = \int_{-\infty}^{0} \chi_\mu(z \leq 0)dz + \int_{0}^{\infty} \chi_\mu(z > 0)dz \tag{3.12}$$

Since $\int_0^\infty \chi_\mu(z > 0)dz$, which corresponds to the scattering of the neutron through the mirror, diverges, we assume that the probability of scattering is small for states with long lifetimes relative to the time scale of the problem and set $\frac{1}{C_n} = \int_{-\infty}^{0} \chi_\mu dz$.

3.2 Simulations

The objective of these simulations will be to clearly differentiate between the classical behavior of particles interacting with curved diffraction planes and the quantum behavior described above. Our aim will be to derive a measure of how we can compare a given set of experimental data to a classical particle model and a quantum wave simulation, and observe the "quantumness" of a given experimental setup. The calculations performed in this section are done for a cylindrical Si/Ni interface mirror, with a radius of curvature of 206.7mm and 8 degrees of arc. However, this model is trivially adapted to any similar configuration.

Particle Behavior

In a particle model, due to the high number of reflections undergone by a particle on a curved surface at low incident angle, we expect that the neutron only reflects off of the curved mirror surface if the angle of impact is lower than the critical angle of the material,

$$\theta_c = \arcsin \frac{n_r}{n_i} \tag{3.13}$$

where n_r and n_i are the indices of refraction of the refractive and incident media, respectively. These indices are given, for a specific material, by Eqn. 1.45. We will consider an incident wavelength of 3.9Å, which corresponds to a typical wavelength for cold neutron experiments. For silicon and nickel, we have

$$n_{Ni} \approx 0.9999780294 \tag{3.14}$$

$$n_{Si} \approx 0.99999518315 \tag{3.15}$$

The critical angle of a ray going from silicon to nickel at 3.9Åis then given by

$$\theta_c = \arcsin \frac{n_{Ni}}{n_{Si}} \approx 89.66^\circ \tag{3.16}$$

This means that rays hitting the surface at an angle of less than 0.34° will be reflected, and others will be transmitted.

For a given experimental configuration, the beam of incident neutrons will have some spatial width, as well as a spread in transverse momentum. The classical behavior of these particles will be estimated by ray tracing, by estimating which trajectories can survive to the detector. The mirror is represented in the x-y plane by $x^2 + y^2 = R^2$, where R is the radius of curvature. The beam is divided into N^2 components, distributed along N starting points within its width, and shooting at N different angles within its spread. For every incident ray, we calculate the point of intersection with the mirror, and calculate the angle of impact between the incident ray and the line tangent to the mirror at this point, given by the derivative of the above equation. If this angle is larger than the critical angle, the beam is transmitted through and lost. If it is lower, the beam is reflected and a new trajectory is calculated, and the process is repeated until it reaches the end of the mirror. Once the beam reaches the exit, its final angle trajectory is recorded.

An example result is shown in figure 3.2. For this simulation, the beam was set to a spatial divergence of 0.14mm, and an angular divergence of 0.5°. These results seem to show that the surviving neutrons are biased towards the low angles, and the resulting distribution is highly asymmetric. This distribution offers a good baseline to which to compare a given experimental dataset.

Quantum (Wave) Behavior

For the mirror used in the above, the quantum mechanical quantities described in section 3.1 are given by:

$$l_0 = (\frac{\hbar^2 R}{2M^2 v^2})^{1/3} = 7.2728 \times 10^{-8} m \tag{3.17}$$

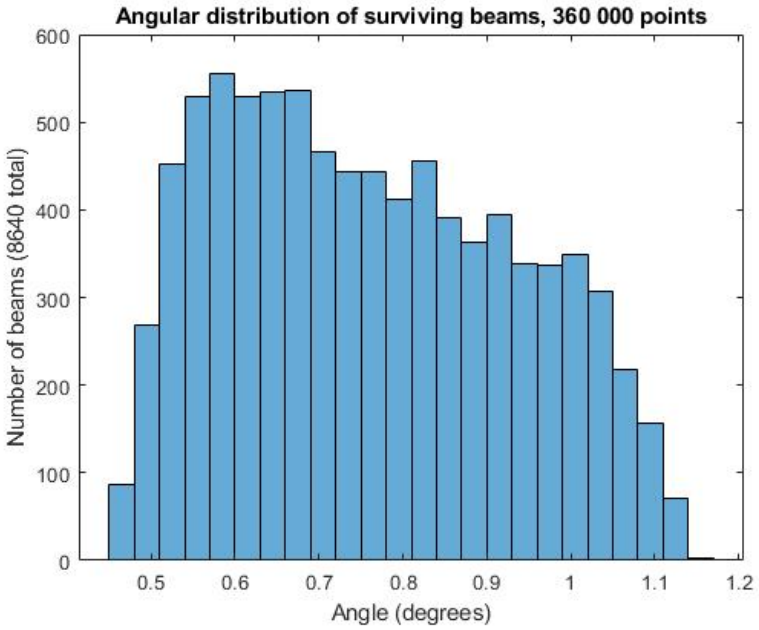

Figure 3.2: A classical simulation of a Si/Ni curved mirror with 206.7mm radius of curvature and measuring 8 degrees of arc. The majority of the surviving paths are transmitted at low angles with respect to the waveguide surface at the exit.

$$\epsilon_0 = (\frac{\hbar^2 M v^4}{2R^2})^{1/3} = 3.918 \times 10^{-9} eV \tag{3.18}$$

$$U_{Ni} = \frac{2\pi\hbar^2 b_{Ni} N_{Ni}}{M} = 2.45 \times 10^{-7} eV \tag{3.19}$$

$$U_{Si} = \frac{2\pi\hbar^2 b_{Si} N_{Si}}{M} = 0.5373 \times 10^{-7} eV \tag{3.20}$$

$$U_0 = \Delta U = U_{Ni} - U_{Si} \approx 191 \times 10^{-9} eV \tag{3.21}$$

$$z_0 = \frac{U_0}{\epsilon_0} = 48.75 \tag{3.22}$$

$$-\frac{\partial U}{\partial x} = \frac{M v^2}{R} \approx 53865 \frac{neV}{mm} \approx -1 \frac{\epsilon_0}{l_0} \tag{3.23}$$

For a typical cold neutron experiment, the neutron wavelength is within the range of 3Å-30Å. Following a previous experiment, we take the mean wavelength to be $\lambda = 3.83$Å, which corresponds to an incoming velocity of $v \approx 1032$ m/s. The energy values are found from $\epsilon_\mu = \lambda_\mu \epsilon_0$ and λ_μ are found by requiring that the states be differentiable at the interface. This is accomplished by numerically solving

$$Ai'(-\lambda_n)(Bi(z_0 - \lambda_\mu) + iAi(z_0 - \lambda_\mu)) = Ai(-\lambda_\mu)(Bi'(z_0 - \lambda_\mu) + iAi'(z_0 - \lambda_\mu))$$

where the prime symbol denotes the first derivative with respect to z. We then find the lifetimes from

$$\Gamma_\mu \approx 4\epsilon_0 \frac{\sqrt{z_0 - \lambda_\mu}}{z_0} \exp -4/3(z_0 - \lambda_\mu)^{3/2} \tag{3.24}$$

and $\tau_\mu = \hbar/\Gamma_\mu$, where τ_μ is the lifetime of state μ. To determine which states contribute to the intensity observed on the detector, the time of flight of the neutron can be estimated classically from the tangential velocity of the neutron (specified by the mean wavelength λ) as well as the arclength of the mirror. To calculate the population of the states, we describe the state of the neutron at the entrance of the mirror as a distribution in radial momentum space. For an incoming beam at incident angle θ and with angular divergence $\delta\phi$, we take

$$\tilde{\Psi}_{beam}(p) = \frac{1}{\sqrt[4]{2\pi\sigma_p^2}} e^{\frac{(p-p_0)^2}{4\sigma_p^2}} \tag{3.25}$$

where

$$p_0 = M v \sin\theta \tag{3.26}$$

$$\sigma_p = M v \sin\delta\phi \tag{3.27}$$

Where θ is the angle of incidence and $\delta\phi$ is the beam angular divergence. The spatial wavefunction corresponding to this momentum distribution is found through a Fourier transform

$$\Psi_{beam}(z) = \frac{1}{\hbar}\int_{-\infty}^{\infty} \tilde{\Psi}_{beam}(p) e^{ipz/\hbar} dp = \frac{1}{\sqrt[4]{2\pi\hbar^2/\sigma_p^2}} e^{ip_0 z/\hbar - \sigma_p^2 z^2/\hbar^2} \tag{3.28}$$

We can then calculate the state populations for a given initial beam from its spectral decomposition

$$\Psi_{beam}(z) = \sum^{\mu} \alpha_\mu \chi_\mu(z) \tag{3.29}$$

where the weights α_μ

$$\alpha_\mu = \int_{-\infty}^{\infty} \Psi_{beam}(z) \chi_\mu^*(z) dz \tag{3.30}$$

Each state then separately acquires a phase along its path in the mirror, according to

$$\Delta\Phi = \frac{1}{\hbar}\int_{\Sigma} \vec{p}\cdot d\vec{s} \tag{3.31}$$

The path inside the mirror can be approximated as purely tangential to the mirror surface, and as such only the tangential component of momentum is considered. The tangential momentum of each quasistationary state can be approximated from the complex (radial) energy of each state

$$p_{tan_\mu} = \sqrt{2ME_{tan_\mu}} = \sqrt{2M(\frac{Mv^2}{2} - \lambda_\mu \epsilon_0)} \tag{3.32}$$

The radial position-space space wavefunction at the end of a mirror of radius R and sustaining an angle ξ is then

$$\Psi_f(z) = \sum^{\mu} W_\mu e^{i\Delta\Phi_\mu} \chi_\mu(z) = \sum^{\mu} \alpha_\mu e^{\frac{iR\xi}{\hbar} p_{tan_\mu}} \Psi_\mu(z) \tag{3.33}$$

The intensity in the far-field will be determined by the (radial) momentum distribution

$$\tilde{\Psi}_f(p) = \frac{1}{\sqrt{2\pi\hbar}}\int_{-\infty}^{\infty} \Psi_f(z) e^{-ipz/\hbar} dz \tag{3.34}$$

The intensity measured at output angle ϕ is then

$$I(\phi) = \tilde{\Psi}_f(Mv\sin\phi)\tilde{\Psi}_f^*(Mv\sin\phi) \tag{3.35}$$

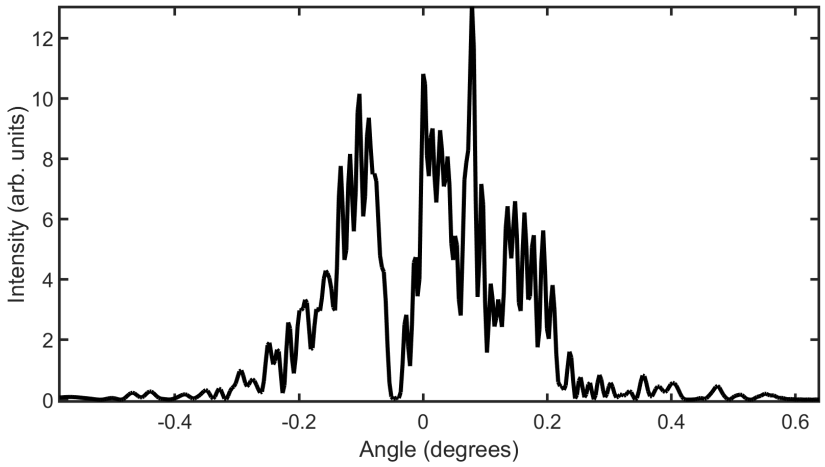

Figure 3.3: The intensity profile in the far-field predicted by the quantum mechanical numerical simulation of a Si/Ni curved mirror with 206.7mm radius of curvature and measuring 8 degrees of arc. The beam wavelength is set to 3.83Å, incident to the mirror surface at 0.05° with 0.01° divergence. Contrarily to the classical simulation, the neutron diffracts to the negative angles, and some angles are forbidden due to destructive interference.

One such result in shown in Fig. 3.3, for the parameters given previously. It can clearly be observed that the quantum profile differs greatly from the classical one. Firstly, positive and negative angles are allowed, which is to be expected naively simply because of the Heisenberg uncertainty. Secondly, some angles are forbidden due to destructive interference between the states, such as in the case of angle $-0.05°$ in our example.

Chapter 4

Conclusions and Future Work

4.1 QI Model for Diffraction

The work presented in this thesis indicates that the QI model for dynamical diffraction is a good match for the existing theory in the Laue and Bragg cases for simple geometries, as well as a good match to experimental data in mixed or complex geometries. This opens many opportunities for the design of neutron optical devices, as it is now easier to account for dynamical diffraction effects when considering the neutron behavior inside perfect crystals. Future work involving this model could include:

1. Designing and modeling neutron optics components that combine dynamical diffraction and phase-grating geometries. A lot of recent interest has been placed on the applications of phase-grating interferometry, where an interference pattern in the far-field is obtained via the grating diffraction orders ([68, 69, 70, 71, 72, 73]). Typical neutron gratings do not consider dynamical diffraction effects, and hence the QI model can be used to rapidly investigate a multitude of different grating parameters such as duty cycle, teeth shape and size, etc.

2. Investigating the effects of impurities and defects in perfect crystal optical instruments. Indeed, the standard theory of DD does not provide a straightforward way to account of imperfections in a general sense. The model offers a simple and intuitive way to model impurities, by replacing individual nodes by vacancies, or adding to them some amount of absorption.

3. Investigating the effects of strains or temperature gradients inside perfect crystal optical devices. Imperfect crystal machining or experimental conditions may induce

some strains inside perfect crystals. Our theory seems to suggest that the changes to the Bragg condition introduced by these strains can be modeled by introducing a gradient of the γ parameter in the crystal.

4. Incorporate spin into the model to account for magnetic field effects, potentially to measure the neutron EDM

5. Designing two-dimensional crystal geometries. For example, neutron orbital angular momentum (OAM) states [19, 22, 74, 75] and spin-coupled OAM states [76, 77, 78] have come to the forefront of neutron science as a potential quantum probe of materials and standard physics. With the QI model we can consider a two-dimensional fork gratings for neutrons to induce neutron OAM through dynamical diffraction. This is would be similar to what was achieved with X-Rays [79].

4.2 Whispering Gallery

In this work, it has been shown that there is a clear difference between the expected particle (ballistic) trajectories of neutrons inside a curved waveguide and the equivalent quantum (wave) behaviour. However, there is a lack of experimental data when it comes to curved waveguides. It would be of general scientific interest to observe these quantum states in different material interfaces, especially in lower potential differences, where there are fewer surviving states and they are well spatially separated.

References

[1] O Nahman-Lévesque, D Sarenac, DG Cory, B Heacock, MG Huber, and DA Pushin. Generalizing the quantum information model for dynamic diffraction. *Physical Review A*, 105(2):022403, 2022.

[2] C. G. Shull. Perfect crystals and imperfect neutrons. *Journal of Applied Crystallography*, 6(4):257–266, Aug 1973.

[3] O. Nahman-Lévesque, D. Sarenac, D. G. Cory, M. G. Huber, and D. A. Pushin. Quantum information approach to the implementation of a neutron cavity. *arXiv preprint arXiv:2208.11098*, 2022.

[4] James Chadwick. Possible existence of a neutron. *Nature*, 129(3252):312–312, 1932.

[5] H Rauch, A Wilfing, W Bauspiess, and U Bonse. Precise determination of the 4π-periodicity factor of a spinor wave function. *Zeitschrift für Physik B Condensed Matter*, 29(3):281–284, 1978.

[6] Clifford Glenwood Shull and J Samuel Smart. Detection of antiferromagnetism by neutron diffraction. *Physical review*, 76(8):1256, 1949.

[7] Arnab Banerjee, Jiaqiang Yan, Johannes Knolle, Craig A Bridges, Matthew B Stone, Mark D Lumsden, David G Mandrus, David A Tennant, Roderich Moessner, and Stephen E Nagler. Neutron scattering in the proximate quantum spin liquid α-rucl3. *Science*, 356(6342):1055–1059, 2017.

[8] Gerald Badurek, Harald Weinfurter, Roland Gähler, Achim Kollmar, Stefan Wehinger, and Anton Zeilinger. Nondispersive phase of the aharonov-bohm effect. *Physical review letters*, 71(3):307, 1993.

[9] Christopher J Wood, Mohamed O Abutaleb, Michael G Huber, Muhammad Arif, David G Cory, and Dmitry A Pushin. Quantum correlations in a noisy neutron interferometer. *Physical Review A*, 90(3):032315, 2014.

[10] AT Yue, MS Dewey, DM Gilliam, GL Greene, AB Laptev, JS Nico, William M Snow, and FE Wietfeldt. Improved determination of the neutron lifetime. *Physical review letters*, 111(22):222501, 2013.

[11] L Koester. Verification of the equivalence of gravitational and inertial mass for the neutron. *Physical Review D*, 14(4):907, 1976.

[12] W Schmatz, T Springer, J t Schelten, and K Ibel. Neutron small-angle scattering: experimental techniques and applications. *Journal of Applied Crystallography*, 7(2):96–116, 1974.

[13] B Jacrot. The study of biological structures by neutron scattering from solution. *Reports on progress in physics*, 39(10):911, 1976.

[14] V Gerold and G Kostorz. Small-angle scattering applications to materials science. *Journal of Applied Crystallography*, 11(5):376–404, 1978.

[15] Julia S Higgins and Richard S Stein. Recent developments in polymer applications of small-angle neutron, x-ray and light scattering. *Journal of Applied Crystallography*, 11(5):346–375, 1978.

[16] J Schelten and Ro W Hendricks. Recent developments in x-ray and neutron small-angle scattering instrumentation and data analysis. *Journal of Applied Crystallography*, 11(5):297–324, 1978.

[17] Tsang Lang Lin, Sow Hsin Chen, N Elise Gabriel, and Mary F Roberts. Small-angle neutron scattering techniques applied to the study of polydisperse rodlike diheptanoylphosphatidylcholine micelles. *Journal of Physical Chemistry*, 91(2):406–413, 1987.

[18] SW Peterson and Henri A Levy. A single-crystal neutron diffraction study of heavy ice. *Acta Crystallographica*, 10(1):70–76, 1957.

[19] Charles W Clark, Roman Barankov, Michael G Huber, Muhammad Arif, David G Cory, and Dmitry A Pushin. Controlling neutron orbital angular momentum. *Nature*, 525(7570):504–506, 2015.

[20] K. Li, M. Arif, D. G. Cory, R. Haun, B. Heacock, M. G. Huber, J. Nsofini, D. A. Pushin, P. Saggu, D. Sarenac, C. B. Shahi, V. Skavysh, W. M. Snow, and A. R. Young. Neutron limit on the strongly-coupled chameleon field. *Phys. Rev. D*, 93:062001, Mar 2016.

[21] D. A. Pushin, M. Arif, and D. G. Cory. Decoherence-free neutron interferometry. *Phys. Rev. A*, 79:053635, May 2009.

[22] Dusan Sarenac, Michael G Huber, Benjamin Heacock, Muhammad Arif, Charles W Clark, David G Cory, Chandra B Shahi, and Dmitry A Pushin. Holography with a neutron interferometer. *Optics express*, 24(20):22528–22535, 2016.

[23] Jürgen Klepp, Stephan Sponar, and Yuji Hasegawa. Fundamental phenomena of quantum mechanics explored with neutron interferometers. *Progress of Theoretical and Experimental Physics*, 2014(8), 2014.

[24] Tobias Denkmayr, Hermann Geppert, Stephan Sponar, Hartmut Lemmel, Alexandre Matzkin, Jeff Tollaksen, and Yuji Hasegawa. Observation of a quantum cheshire cat in a matter-wave interferometer experiment. *Nature communications*, 5:4492, 2014.

[25] Roberto Colella, Albert W Overhauser, and Samuel A Werner. Observation of gravitationally induced quantum interference. *Physical Review Letters*, 34(23):1472, 1975.

[26] Yuji Hasegawa and Helmut Rauch. Quantum phenomena explored with neutrons. *New Journal of Physics*, 13(11):115010, 2011.

[27] DA Pushin, MG Huber, M Arif, CB Shahi, J Nsofini, CJ Wood, D Sarenac, and DG Cory. Neutron interferometry at the national institute of standards and technology. *Advances in High Energy Physics*, 2015:1–6, 2015.

[28] CB Shahi, M Arif, DG Cory, T Mineeva, J Nsofini, D Sarenac, CJ Williams, MG Huber, and DA Pushin. A new polarized neutron interferometry facility at the ncnr. *Nuclear Instruments and Methods in Physics Research Section A: Accelerators, Spectrometers, Detectors and Associated Equipment*, 813:111–122, 2016.

[29] Michael G Huber, Shannon F Hoogerheide, Muhammad Arif, Robert W Haun, Fred E Wietfeldt, Timothy C Black, Chandra B Shahi, Benjamin Heacock, Albert R Young, Ivar AJ Taminiau, et al. Overview of neutron interferometry at nist. In *EPJ Web of Conferences*, volume 219, page 06001. EDP Sciences, 2019.

[30] J-M Sparenberg and Helmut Leeb. Neutron charge radius deduced from bragg reflection technique. *Physical Review C*, 66(5):055210, 2002.

[31] J-M Sparenberg and Helmut Leeb. Neutron–electron scattering length deduced from pendellösung interferometry in neutron bragg reflections on silicon. *Journal of electron spectroscopy and related phenomena*, 129(2-3):315–317, 2003.

[32] Benjamin Heacock, Takuhiro Fujiie, Robert W. Haun, Albert Henins, Katsuya Hirota, Takuya Hosobata, Michael G. Huber, Masaaki Kitaguchi, Dmitry A. Pushin, Hirohiko Shimizu, Masahiro Takeda, Robert Valdillez, Yutaka Yamagata, and Albert R. Young. Pendellösung interferometry probes the neutron charge radius, lattice dynamics, and fifth forces. *Science*, 373(6560):1239–1243, 2021.

[33] Shigeyasu Itoh, Masaya Nakaji, Yuya Uchida, Masaaki Kitaguchi, and Hirohiko M. Shimizu. Pendellösung interferometry by using pulsed neutrons. *Nuclear Instruments and Methods in Physics Research Section A: Accelerators, Spectrometers, Detectors and Associated Equipment*, 908:78–81, 2018.

[34] AI Ioffe, VS Zabiyakin, and GM Drabkin. Test of a diffraction grating neutron interferometer. *Physics Letters A*, 111(7):373–375, 1985.

[35] Manfred Gruber, Kurt Eder, Anton Zeilinger, Roland Gähler, and Walter Mampe. A phase-grating interferometer for very cold neutrons. *Physics Letters A*, 140(7-8):363–367, 1989.

[36] G Van der Zouw, M Weber, J Felber, R Gähler, P Geltenbort, and A Zeilinger. Aharonov–bohm and gravity experiments with the very-cold-neutron interferometer. *Nuclear Instruments and Methods in Physics Research Section A: Accelerators, Spectrometers, Detectors and Associated Equipment*, 440(3):568–574, 2000.

[37] Uwe Schellhorn, Romano A Rupp, Stefan Breer, and Roland P May. The first neutron interferometer built of holographic gratings. *Physica B: Condensed Matter*, 234:1068–1070, 1997.

[38] J Klepp, Christian Pruner, Y Tomita, C Plonka-Spehr, P Geltenbort, S Ivanov, G Manzin, KH Andersen, J Kohlbrecher, MA Ellabban, et al. Diffraction of slow neutrons by holographic sio 2 nanoparticle-polymer composite gratings. *Physical Review A*, 84(1):013621, 2011.

[39] MR Eskildsen, PL Gammel, ED Isaacs, C Detlefs, K Mortensen, and DJ Bishop. Compound refractive optics for the imaging and focusing of low-energy neutrons. *Nature*, 391(6667):563–566, 1998.

[40] HR Beguiristain, IS Anderson, CD Dewhurst, MA Piestrup, JT Cremer, and RH Pantell. A simple neutron microscope using a compound refractive lens. *Applied physics letters*, 81(22):4290–4292, 2002.

[41] Charles K Gary. Compound refractive lenses for thermal neutron applications. Technical report, Adelphi Technology, Inc., 2013.

[42] T Oku and HM Shimizu. Neutron lens and prism. *Physica B: Condensed Matter*, 283(4):314–317, 2000.

[43] Masako Yamada. Development and application of a magnetic neutron lens with modulating permanent magnet sextupole. 2015.

[44] KC Littrell, SGE Te Velthuis, GP Felcher, S Park, BJ Kirby, and MR Fitzsimmons. Magnetic compound refractive lens for focusing and polarizing cold neutron beams. *Review of scientific instruments*, 78(3):035101, 2007.

[45] HM Shimizu, T Oku, H Sato, C Otani, H Kato, Y Suda, H Nakagawa, T Kamiyama, Y Kiyanagi, and T Wakabayashi. A magnetic neutron lens. *Physica B: Condensed Matter*, 276:63–64, 2000.

[46] SS Arzumanov, LI Govor, VI Morozov, Yu N Panin, and AN Strepetov. A convergent neutron lens based on glass capillaries. *Instruments and Experimental Techniques*, 59(5):650–652, 2016.

[47] MA Kumakhov and VA Sharov. A neutron lens. *Nature*, 357(6377):390–391, 1992.

[48] Huarui Wu, Boris Khaykovich, Xuewu Wang, and Daniel S Hussey. Wolter mirrors for neutron imaging. *Physics Procedia*, 88:184–189, 2017.

[49] C Kapahi, D Sarenac, M Bleuel, DG Cory, B Heacock, M Henderson, MG Huber, I Taminiau, and DA Pushin. Next-generation high transmission neutron optical devices utilizing micro-machined structures. *arXiv preprint arXiv:2112.13176*, 2021.

[50] J. Nsofini, K. Ghofrani, D. Sarenac, D. G. Cory, and D. A. Pushin. Quantum-information approach to dynamical diffraction theory. *Physical Review A*, 94(6), Dec 2016.

[51] John Von Neumann. Mathematical foundations of quantum mechanics. In *Mathematical Foundations of Quantum Mechanics*. Princeton university press, 2018.

[52] Subrahmanyan Chandrasekhar. Stochastic problems in physics and astronomy. *Reviews of modern physics*, 15(1):1, 1943.

[53] Albert Einstein. *Investigations on the Theory of the Brownian Movement*. Courier Corporation, 1956.

[54] G.H. Weiss and G.H. Weiss. *Aspects and Applications of the Random Walk*. International Congress Series. North-Holland, 1994.

[55] J Kempe. Quantum random walks: An introductory overview. *Contemporary Physics*, 44(4):307–327, jul 2003.

[56] Helmut Rauch and Samuel A Werner. *Neutron interferometry: lessons in experimental quantum mechanics*. Oxford University Press, New York, 2015.

[57] John M Cowley and A F_ Moodie. The scattering of electrons by atoms and crystals. i. a new theoretical approach. *Acta Crystallographica*, 10(10):609–619, 1957.

[58] WHt Zachariasen. A general theory of x-ray diffraction in crystals. *Acta Crystallographica*, 23(4):558–564, 1967.

[59] NORIO Kato. Statistical dynamical theory of crystal diffraction. ii. intensity distribution and integrated intensity in the laue cases. *Acta Crystallographica Section A: Crystal Physics, Diffraction, Theoretical and General Crystallography*, 36(5):770–778, 1980.

[60] S. A. Werner, R. R. Berliner, and M. Arif. Mathematical methods in the solution of the Hamilton-Darwin and the Takagi-Taupin equations. *Physica B+C*, 137(1):245–255, March 1986.

[61] C. G. Shull. Observation of pendellösung fringe structure in neutron diffraction. *Phys. Rev. Lett.*, 21:1585–1589, Dec 1968.

[62] Joachim Nsofini, Dusan Sarenac, Kamyar Ghofrani, Michael G Huber, Muhammad Arif, David G Cory, and Dmitry A Pushin. Noise refocusing in a five-blade neutron interferometer. *Journal of Applied Physics*, 122(5):054501, 2017.

[63] J Nsofini, D Sarenac, DG Cory, and DA Pushin. Coherence optimization in neutron interferometry through defocusing. *Physical Review A*, 99(4):043614, 2019.

[64] Noam Chomsky and Marcel P Schützenberger. The algebraic theory of context-free languages. In *Studies in Logic and the Foundations of Mathematics*, volume 26, pages 118–161. Elsevier, 1959.

[65] Yu G Abov, NO Elyutin, and AN Tyulyusov. Dynamical neutron diffraction on perfect crystals. *Physics of Atomic Nuclei*, 65(11):1933–1979, 2002.

[66] VV Nesvizhevsky, AK Petukhov, KV Protasov, and A Yu Voronin. Centrifugal quantum states of neutrons. *Physical Review A*, 78(3):033616, 2008.

[67] E Gerjuoy. Outgoing boundary condition in rearrangement collisions. *Physical Review*, 109(5):1806, 1958.

[68] Huseyin Ekinci, Bo Cui, and Dmitry Pushin. Fabrication of sub-micron trenches with surfactant-added koh. In *2020 IEEE 20th International Conference on Nanotechnology (IEEE-NANO)*, pages 172–175, 2020.

[69] Dmitry A Pushin, Dusan Sarenac, Daniel S Hussey, Haixing Miao, Muhammad Arif, David G Cory, Michael G Huber, David L Jacobson, Jacob M LaManna, Joseph D Parker, et al. Far-field interference of a neutron white beam and the applications to noninvasive phase-contrast imaging. *Physical Review A*, 95(4):043637, 2017.

[70] Dusan Sarenac, Dimitry A Pushin, Michael G Huber, Daniel S Hussey, Haixing Miao, Muhammad Arif, David G Cory, Alexander D Cronin, Benjamin Heacock, David L Jacobson, et al. Three phase-grating moiré neutron interferometer for large interferometer area applications. *Physical review letters*, 120(11):113201, 2018.

[71] Daniel S Hussey, Houxun Miao, Guangcui Yuan, Dmitry Pushin, Dusan Sarenac, Michael G Huber, David L Jacobson, Jacob M LaManna, and Han Wen. Demonstration of a white beam far-field neutron interferometer for spatially resolved small angle neutron scattering. *arXiv preprint arXiv:1606.03054*, 2016.

[72] B Heacock, D Sarenac, DG Cory, MG Huber, DS Hussey, C Kapahi, H Miao, H Wen, and DA Pushin. Angular alignment and fidelity of neutron phase-gratings for improved interferometer fringe visibility. *AIP Advances*, 9(8):085115, 2019.

[73] B Heacock, D Sarenac, DG Cory, MG Huber, JPW MacLean, H Miao, H Wen, and DA Pushin. Neutron sub-micrometre tomography from scattering data. *IUCrJ*, 7(5):893–900, 2020.

[74] D. Sarenac, M. E. Henderson, H. Ekinci, Charles W. Clark, D. G. Cory, L. Debeer-Schmitt, M. G. Huber, C. Kapahi, and D. A. Pushin. Experimental realization of neutron helical waves, 2022.

[75] Dusan Sarenac. Structured beams as quantum probes. 2018.

[76] Joachim Nsofini, Dusan Sarenac, Christopher J Wood, David G Cory, Muhammad Arif, Charles W Clark, Michael G Huber, and Dmitry A Pushin. Spin-orbit states of neutron wave packets. *Physical Review A*, 94(1):013605, 2016.

[77] D Sarenac, J Nsofini, I Hincks, M Arif, Charles W Clark, DG Cory, MG Huber, and DA Pushin. Methods for preparation and detection of neutron spin-orbit states. *New journal of physics*, 20(10):103012, 2018.

[78] Dusan Sarenac, Connor Kapahi, Wangchun Chen, Charles W Clark, David G Cory, Michael G Huber, Ivar Taminiau, Kirill Zhernenkov, and Dmitry A Pushin. Generation and detection of spin-orbit coupled neutron beams. *Proceedings of the National Academy of Sciences*, 116(41):20328–20332, 2019.

[79] Justin S Woods, Xiaoqian M Chen, Rajesh V Chopdekar, Barry Farmer, Claudio Mazzoli, Roland Koch, Anton S Tremsin, Wen Hu, Andreas Scholl, Steve Kevan, et al. Switchable x-ray orbital angular momentum from an artificial spin ice. *Physical review letters*, 126(11):117201, 2021.